



School of Mechanical and Manufacturing Engineering

Faculty of Engineering

UNSW Sydney

BY

Benjamin McMillen

Low Power Energy Harvesting System for Underwater Beacons on ROVs

Thesis submitted as a requirement for the degree of Bachelor of Engineering in
Mechatronic Engineering

Submitted: 08/08/2025

Student zID: z5363575

Supervisor: Will Midgley (UNSW)

ORIGINALITY STATEMENT

'I hereby declare that this submission is my own work and to the best of my knowledge it contains no materials previously published or written by another person, or substantial proportions of material which have been accepted for the award of any other degree or diploma at UNSW or any other educational institution, except where due acknowledgement is made in the thesis. Any contribution made to the research by others, with whom I have worked at UNSW or elsewhere, is explicitly acknowledged in the thesis. I also declare that the intellectual content of this thesis is the product of my own work, except to the extent that assistance from others in the project's design and conception or in style, presentation and linguistic expression is acknowledged.'

Signed



Date 08/08/2025

Abstract

This thesis presents the development of a compact, omnidirectional piezoelectric energy harvesting system for underwater use on remotely operated vehicles. Traditional PEHS are often bulky and optimised for omnidirectional flow, which in turn limits their effectiveness in dynamic ocean environments. The thesis proposes a design that addresses these limitations by harvesting energy along a plane from currents in any direction, while maintaining an overall design that has minimal impact on the motion and control of the system. Harvested energy will power a beacon to aid in the recovery of malfunctioning vehicles, providing an alternative to standard battery-dependent systems.

Acknowledgements

I would like to express my sincere gratitude to my thesis supervisor, Dr. Will Midgley, for his continued support, guidance, and valuable feedback throughout the course of this project. His insight and encouragement were instrumental to the development and completion of this work. I would also like to thank Nathan Sivalingam for his assistance with formatting and ensuring the presentation of this thesis met the required standards. Special thanks to Hazel McMillen for generously offering her time to review my work and provide thoughtful corrections and suggestions. Finally, I acknowledge the use of Grammarly, which proved helpful for spell-checking and minor grammatical corrections.

Contents

Abstract.....	iii
Acknowledgements.....	iv
Contents	v
List of Figures.....	viii
List of Tables	xii
Nomenclature.....	xii
1 Introduction	1
2 Literature review	3
2.1 Current Technologies in AUV Failsafes and Use Cases for Underwater Energy Harvesting	3
2.1.1 Current Failsafe for Underwater ROVs	3
2.1.2 Energy Harvesting from the Ocean.....	3
2.2 Fundamentals of Piezoelectric Energy Harvesting	4
2.2.1 Piezoelectric Energy Harvesters	4
2.2.2 Materials Used for PEH	5
2.2.3 Energy Conversion Process.....	5
2.3 Vortex-Induced Vibrations.....	6
2.3.1 Vortex-Induced Vibrations and Karmen Vortex Streets	6
2.3.2 Bluff Body Shapes/Effects of Blockage Ratio on VIV.....	7
2.3.3 Effect of Submergence Depth on VIV	7
2.4 Piezoelectric Energy Harvester Designs	8
2.4.1 Low Speed PEHs.....	8
2.4.2 PEHs Harvesting through a Single Flow	8
2.4.3 PEHs with Multiple Degrees of Freedom.....	9
2.4.4 Positioning of Bluff Bodies Relative to Air Flow and Energy Harvesters	14
2.4.5 Effects of Bluff Body Shapes/Cross-sections on Piezoelectric Energy Harvesters	15
2.4.6 Single Bluff Body Vs Implementation of a Separate Bluff Body.....	19
2.5 Concluded Gaps in Literature	20

3	Methodology.....	21
3.1	M1 - Validation of Simulation Accuracy and Previous Report Analysis	21
3.1.1	Selection of PEH Design Type	21
3.1.2	Mode Shape and Natural Frequency Extraction Process	21
3.1.3	Analysis of Existing Design Vortex Shedding Frequencies	22
3.1.4	Setup for Power Output Simulation	24
3.2	M2 - Design and Simulation of Single-PEH.....	24
3.2.1	Dimension and Sizing Considerations	25
3.2.2	Bluff Body Vortex Frequency Measurements and Material Selection	25
3.2.3	Power Output Simulation Under Laminar Flow	26
3.3	M3 - Design and Simulation of Multi-PEH	26
3.3.1	Spacing Strategy and Arrangement Configuration	26
3.3.2	Setup for Multi-Body Coupled Simulations	27
3.4	M4 - Design and Testing of Multi-PEH Container/Shell.....	28
3.4.1	Shell Design Considerations for Dimensions and Sizing	28
3.4.2	Shell Material and Shape Considerations	28
3.4.3	Simulation Process for Drag Testing of Shell.....	29
4	Results and discussion.....	30
4.1	M1 - Validation of Simulation Accuracy and Previous Report Analysis	30
4.1.1	Justification for Selected PEH Type	30
4.1.2	Validation of Modal Behaviour and Natural Frequencies of Existing Design	30
4.1.3	Alignment with Vortex Shedding Frequencies	32
4.1.4	Simulated Peak Power Performance and Verification	33
4.2	M2 - Design and Simulation of Single-PEH.....	34
4.2.1	Design Decisions regarding Dimensions and Sizing	34
4.2.2	Bluff Body Vortex Frequency and Evaluation of Candidate Designs Frequencies.....	35
4.2.3	Comparative Power Output of Candidate Designs	36
4.3	M3 - Design and Simulation of Multi-PEH	38

B. McMillen – Low Power Energy Harvesting System for Underwater Beacons on ROVs

4.3.1	Effect of Spacing on PEH Power Output.....	38
4.3.2	Simulated Power Output for Multiple PEH Configurations	39
4.4	M4 - Design and Testing of Multi-PEH Container/Shell.....	45
4.4.1	Shell Design Decisions Regarding Dimensions and Sizing.....	45
4.4.2	Shell Material and Shape Selection.....	45
4.4.3	Results of Drag Simulation Testing	46
4.5	Discussion	48
5	Conclusions	49
6	References	51
7	Appendices	53
	Appendix A.....	53
	Appendix B	54
	Appendix C	55
	Appendix D.....	56
	Appendix E	60
7.1.1	15 mm Diameter Singular PEHs Velocity Contours.....	60
7.1.2	10 mm Diameter PEHs Velocity Contours	61
	Appendix F	63
7.1.3	2D Separations	63
7.1.4	3D Separations	64
7.1.5	4D Separations	66

List of Figures

Figure 1 - Flow Chart of Project Milestones	2
Figure 2 - Compression-based PEH Diagram [9].....	4
Figure 3 - Diagram of Vortices Produced by VIV of a Circular Cross-section Bluff Body [13].....	6
Figure 4 – Diagram of Magnetically Coupled PEH with Cantilever Beam [19].....	8
Figure 5 – 2DOF Wind PEH Bending Diagrams [24].....	9
Figure 6 – 2DOF Wind PEH with the Addition of a Magnet [25]	10
Figure 7 – Impacting Pendulum PEH Diagram [27]	11
Figure 8 – Impacting Pendulum PEH from the VIV Diagram [28]	11
Figure 9 – MEMS PEH Design with Two Forms of Deformation [29]	12
Figure 10 - Two-directional Wind-based Cantilever PEH [30].....	13
Figure 11 – Graph of Electrical Output Comparison of S-DOF and H-Shape PEH [31].....	14
Figure 12 – (a) Graph Representing Voltage Output at Different Distance Ratios, (b) Graph Representing Power Output at Different Distance Ratios [32].....	14
Figure 13 - Schematic Drawing of MEMS PEH [29].....	15
Figure 14- Diagram of U-shaped Bluff Body Setup for PEH in Pipe [21].....	16
Figure 15 – Graph Comparing the Power Output of Cylindrical-shaped and U-shaped Bluff Bodies at Different Lengths [21]	17
Figure 16 - Diagram of the Most Effective Bluff Body Cross-section Shape from [35]	17
Figure 17 – Diagram Comparing Velocity and Total Pressure Flows of Different Hybrid Bluff bodies [36]	18
Figure 18 – Experimental Setup of Piezoelectric Energy Harvester and Corresponding Rod Placement Locations [37]	18
Figure 19 – Graph Comparing Energy Efficiencies with Different Rod Placements to Flow Rate [37]	19
Figure 20 - ANSYS Workbench Simulation Setup for Natural Frequencies and Mode Shapes.....	22
Figure 21 - Example 2D CAD Sketch Representing the Cross-sectional Area of the Bluff Body	22
Figure 22 – a) Example Lift Force Vs Time Graph on Bluff Body Cross-section b) Fourier Transformation of Lift force vs Time.....	23
Figure 23 – ANSYS Workbench Two-way Coupled Simulation Setup.....	23
Figure 24 - Example Single PEH Velocity Contour With Cylindrical Bluff Body.....	26
Figure 25 - Example Three-by-Three CAD Model with Separation of 2D.....	27
Figure 26 - BlueROV2 Important Dimensions.....	28
Figure 27 - Perpendicular MEMS PEH [29]	30
Figure 28 - CAD Model for 2mm Diameter PEH	31

Figure 29 - Bending Mode of Deformation 55.278 Hz	31
Figure 30 - Torsional Mode of Deformation 135.25 Hz	32
Figure 31 – Two-way Coupled Simulation showing Velocity of Flow Past PEH, Top-down View	32
Figure 32 – Two-way Coupled Simulation showing Velocity of Flow Past PEH, Angled View	33
Figure 33 - Power Output vs Flow Rate of MEMS PEH [29]	33
Figure 34 - Power Output vs Time for Simulated MEMS PEH	34
Figure 35 - a) 10mm Diameter PEH CAD Model b) 15mm Diameter PEH CAD Model	35
Figure 36 - 10 and 15mm PEH Power Output vs Flow Rate.....	37
Figure 37 - Velocity Contours for Tested single PEH Configurations.....	38
Figure 38 - Diagram Demonstrating L and D in Relation to PEH Bluff Bodies for a Three-by-Three Configuration.....	39
Figure 39 - Power Output vs Flow Rate for PEH Configurations	40
Figure 40 - Velocity Contours for Evaluated Multi-PEH Configurations.....	41
Figure 41 - Small-scale Arrangement of how PEHs will be Arranged	42
Figure 42 - Entire Multi-PEH Layout for Overall ROV	43
Figure 43 - Graph for Power Output vs Current Flow Rate for Multi-PEH Systems	44
Figure 44 - a) PEH Shell Front View b) PEH Shell Side View.....	45
Figure 45 - CAD Model used for Drag Testing.....	47
Figure 46 – Example Fluid Path Lines for Drag Simulations	48
Figure 47 – VIV Lift Force at 0.1m/s, 15mm Diameter	56
Figure 48 – ANSYS Fourier Analysis for VIV Frequency at 0.1m/s, 15mm Diameter.....	56
Figure 49 – VIV Lift Force at 0.5m/s, 15mm Diameter	57
Figure 50 – ANSYS Fourier Analysis for VIV Frequency at 0.5m/s, 15mm Diameter.....	57
Figure 51 – VIV Lift Force at 0.1m/s, 10mm Diameter	58
Figure 52 – ANSYS Fourier Analysis for VIV Frequency at 0.1m/s, 10mm Diameter.....	58
Figure 53 – VIV Lift Force at 0.5m/s, 10mm Diameter	58
Figure 54– ANSYS Fourier Analysis for VIV Frequency at 0.5m/s, 10mm Diameter.....	59
Figure 55 – 0.1m/s Flow Rate, 15mm Diameter Cylinder	60
Figure 56 – 0.3m/s Flow Rate, 15mm Diameter Cylinder	60
Figure 57 – 0.1m/s Flow Rate, 15mm Diameter Cylinder	61
Figure 58 – 0.1m/s Flow Rate, 10mm Diameter Cylinder	61
Figure 59 – 0.3m/s Flow Rate, 10mm Diameter Cylinder	62
Figure 60 – 0.5m/s Flow Rate, 10mm Diameter Cylinder	62
Figure 61 - 0.1m/s Flow rate, 10mm Diameter Cylinder, Three-by-Three 2D Separation	63

Figure 62 - 0.3m/s Flow rate, 10mm Diameter Cylinder, Three-by-Three 2D Separation	63
Figure 63 - 0.5m/s Flow rate, 10mm Diameter Cylinder, Three-by-Three 2D Separation	64
Figure 64 - 0.1m/s Flow Rate, 10mm Diameter Cylinder, Three-by-Three 3D Separation.....	64
Figure 65 – 0.3m/s Flow Rate, 10mm Diameter Cylinder, Three-by-Three 3D Separation	65
Figure 66 - 0.5m/s Flow Rate, 10mm Diameter Cylinder, Three-by-Three 3D Separation.....	65
Figure 67 - 0.1m/s Flow Rate, 10mm Diameter Cylinder, Three-by-Three 4D Separation.....	66
Figure 68 - 0.3m/s Flow Rate, 10mm Diameter Cylinder, Three-by-Three 4D Separation.....	66
Figure 69 - 0.5m/s Flow Rate, 10mm Diameter Cylinder, Three-by-Three 4D Separation.....	67

List of Tables

Table 1 - Comparing Maximum Voltages for Different SDOF and 2 SDOF PEH Systems [33].....	20
Table 2 - Natural Frequencies Depending on Materials	36
Table 3 - Power Output for 10mm and 15mm Bluff Body Diameter PEHs.....	36
Table 4 - Multi-PEH Power Output.....	39
Table 5 - Power Output for Forward and Backward Current Flow	44
Table 6 - Power Output for Sideways Current Flow	44
Table 7 – Comparison of Material Properties.....	46
Table 8 - Simulated Drag for Shell and Calculated Drag for ROV at Varying Flow Rates.....	47
Table 9- Single PEH Dimensions	54
Table 10 - VIV Frequency for 0.1m/s to 0.5m/s Water Flow.....	55

Nomenclature

A	= Amplitude of VIV response
Ar	= Area of piezoelectric material
C	= Capacitance
d	= distance between bluff body and PEH
d_{ij}	= piezoelectric coefficient
D	= Diameter of bluff body
E	= Young's modulus
f	= Frequency of applied force
F	= Force applied to the piezoelectric material
H	= Separation distance between upper and lower walls.
L	= characteristic linear dimension
P	= Power output
R	= Resistance
Re	= Reynolds number
St	= Strouhal number
u	= flow speed of fluid
V	= Voltage
β	= Blockage ratio D/H
μ	= dynamic viscosity of the fluid
ρ	= density of fluid
DOF	= Degree of Freedom
DPEH	= Double Piezoelectric energy harvester
EH-WSN	= Energy Harvesting Wireless Sensor Network
FIV	= Flow-Induced Vibrations
MEMS	= Micro-electromechanical system
PEH	= Piezoelectric energy harvester
PVDF	= Polyvinylidene Fluoride
PZT	= Lead Zirconate Titanate
ROV	= Remote Operated Vehicle
UWSN	= Underwater Wireless Sensor Network
VIV	= Vortex Induced Vibrations
WSN	= Wireless Sensor Network

1 Introduction

Underwater technologies such as autonomous underwater vehicles (AUVs) and underwater wireless sensor networks (UWSNs) play a critical role in providing a wide range of applications, including ocean exploration, underwater navigation, communication technologies, and environmental monitoring. As the oceans cover the vast majority of the Earth's surface, understanding and researching the oceans is essential for various areas, including scientific research, environmental and resource management, as well as the security of different regions. AUVs and UWSNs are a significant focus in the management and development of these operations, allowing real-time data to be effectively and efficiently collected from areas that were previously inaccessible. However, AUVs are expensive and operate in harsh, hard-to-reach environments, making recovery in the event of failure difficult and costly. This problem has led to increased interest in the development of energy-autonomous systems capable of extending operational life or assisting in recovery procedures without relying solely on conventional battery systems.

Furthermore, recent advancements in piezoelectric energy harvesters (PEHs) have enabled their application in self-powered sensors and adaptive energy harvesters, often harvesting energy through the vibration of mechanical systems or the flow of fluids due to their ability to generate small amounts of energy via the utilisation of small quantities of piezoelectric materials. Among these, underwater fluid-induced vibrations (FIV), especially vortex-induced vibrations (VIV) caused by vortex shedding around bluff bodies, have been widely studied for their potential in low-power energy generation. However, most current PEH designs are optimised for unidirectional, consistent flows such as those in pipelines, which are not representative of the highly variable and multidirectional nature of ocean currents.

The project will focus on the design and development of a compact PEH system optimised for the dynamic underwater environments encountered by AUVs, specifically the BlueROV2 remotely operated vehicle (ROV). Unlike conventional designs, which often occupy a significant amount of vertical space, this design will be constrained in height to ensure its compatibility with the ROV. The energy harvester will act along a plane to enable omnidirectional sensitivity to ocean currents and is intended to power a low-power underwater beacon. This beacon can assist in the localisation and potential recovery of a malfunctioning AUV or ROV by remaining operational even if the host vehicle fails to power it.

The reliability and survivability of underwater systems are dependent on their ability to generate power from the surrounding underwater environment autonomously. Battery-powered beacons are limited by their capacities and may fail before recovery efforts have been completed. A robust, compact PEH system that induces minimal effects on the motion of an ROV capable of harvesting energy from fluid flow in multiple directions provides a sustainable

solution for the long-term operation and emergency signalling of the device. By addressing the limitations of current PEH designs, specifically their size and directional dependency, this project contributes to the development of more resilient underwater systems, resulting in enhanced mission success rates, reduced recovery costs, and improved data preservation in the event of underwater system failure.

To achieve this goal, the project is divided into four main milestones. The first milestone involves determining and recreating the results of an optimal PEH design based on the specific criteria of the situation through CAD and CFD simulations. This validates the results of Milestones two and three and establishes a suitable PEH type. Second, the design of a singular PEH device that harvests energy effectively in the given underwater current will be developed based on the previous device. Milestone three involves the testing of this singular PEH design in a multi-PEH situation to determine the most optimal configuration of PEHs for energy harvesting. Finally, the overall outer shell, which holds all the PEHs and is fixed to the ROV, is designed and tested to minimise its impact on the ROV's motion. These milestones are further visually demonstrated in the flow chart of Figure 1.

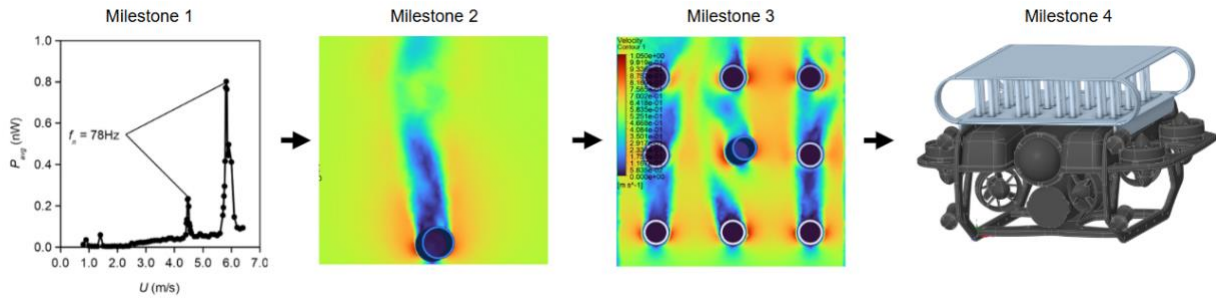


Figure 1 - Flow Chart of Project Milestones

2 Literature review

2.1 Current Technologies in AUV Failsafes and Use Cases for Underwater Energy Harvesting

2.1.1 Current Failsafe for Underwater ROVs

Current solutions to the problem of underwater ROVs being difficult to recover revolve around the use of battery-powered underwater emergency locator beacons, with some, such as the ULB-362PL, implementing electrical systems that activate only upon ROV power loss, using a relay that is directly connected to the ROV's power source [1]. Other beacons, such as the ULB-362 [1] and the more cost-effective ULB-364 [2] are often activated when in contact with water, causing them to continuously ping the ROV's current location for both general localisation and emergencies. The lifespan of these beacons ranges from 30 to 90 days; thus, for continuous reuse or long-term implementation of ROV technology, the powering of such beacons may fail due to battery depletion or human error. For long-term AUV missions or continuous AUV use, batteries often become unreliable. Therefore, the design of a device that continuously harvests energy from the surrounding underwater environment would be ideal to guarantee the AUV is always locatable. The ULB-362 uses a single 6V lithium battery while the ULB-364 uses two 9V alkaline batteries. For the two 9V alkaline batteries, a rough power consumption can be calculated as 4.17mW for a maximum 90-day mission while using the ULB-364, as shown in Appendix A.

Furthermore, a different low-power communication and localisation device for underwater micro-AUVs is highlighted in [3]. The power consumption for this design was on average 300 mW in sleep mode, while during transmission, the power consumption could rise to 2.1W. This device was able to transmit over ranges of up to a few hundred metres [3]. This assists in establishing a goal for power production in the energy harvesting system being designed for similar devices.

Other existing failsafes for underwater ROVs, which do not primarily involve the use of beacons, rely strongly on the device being able to detect these critical situations and then surface once these emergencies occur [4]. These mechanisms rely on the device being able to surface independently, meaning that the surfacing mechanisms must remain functional and powered to achieve the desired outcome. Again, these surfacing mechanisms are directly attached to the AUV's power source, meaning that failures could still occur if the battery malfunctions.

2.1.2 Energy Harvesting from the Ocean

The use of energy harvesting systems is common in devices or systems that require wireless operation due to the difficulty and expense of establishing and maintaining wired networks in isolated locations, such as the ocean. Such devices include EH-WSNs and the emergency distress signalling of underwater ROVs. Currently, above-water EH-WSNs rely primarily on the use of radiant energy from solar cells; however, recently, the use of piezoelectric energy

harvesters (PEHs) has become more viable in harvesting energy from vibrating systems, providing a power density of $960\text{nW}/\text{cm}^3$ from acoustic noise and $330\mu\text{W}/\text{cm}^3$ from motion [5].

For UWSNs, harvesting energy from a mechanical source, such as the vibration of a wave or flow from an underwater current, is commonly generated through the implementation of piezoelectric energy harvesters, which rely on the vortices produced by these sources. This is because they provide a higher voltage of energy without the need for any external supplies [6]. Furthermore, the lack of electromagnetic interference and low cost make PEHs relatively easy to model in UWSNs [6]. Conventionally, the source of power in these UWSNs uses batteries; however, their shorter life and low capacity limit their functionality and effectiveness. Instead, the use of super capacitors and rechargeable batteries to store the harvested energy reduces the maintenance and increases the effectiveness of these UWSNs [6].

2.2 Fundamentals of Piezoelectric Energy Harvesting

2.2.1 Piezoelectric Energy Harvesters

“The piezoelectric effect describes the capability of certain materials to generate spatially separated opposite electrical charges in response to mechanical deformation produced by an external force” [7]. The internal structure of piezoelectric materials includes regions called electrical dipoles, which are microscopic charge separations consisting of positive and negative charge centres. When these piezoelectric materials are put under mechanical stress, the position and arrangement of these electrical dipoles are slightly displaced, resulting in the redistribution of the charge centres and hence leading to the generation of an electrical charge on the surface of the piezoelectric material, which can then be harnessed [8]. PEHs utilise this phenomenon to convert ambient mechanical energies, such as pressure or vibrations of a system, into a usable electrical energy, as outlined in Figure 2 which highlights how compression of a piezoelectric material can produce an electrical output.

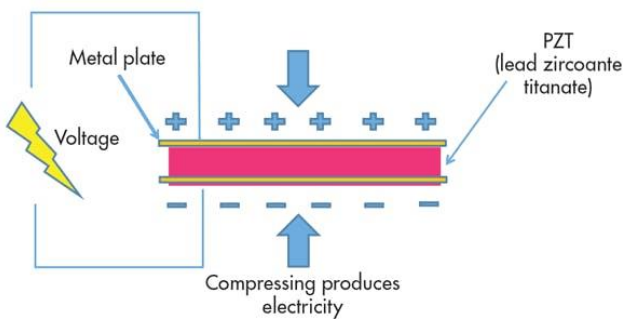


Figure 2 - Compression-based PEH Diagram [9]

2.2.2 Materials Used for PEH

The piezoelectric material used in a PEH significantly influences the effectiveness and efficiency of the overall PEH device. Some commonly used piezoelectric materials include, but are not limited to, PZT, PVDF and piezoelectric composites. These different types of piezoelectric materials exhibit varying properties and are therefore suitable for use in various applications.

PZT is a piezoelectric material that generates high amounts of electrical charge for the given mechanical stress applied to it, as it has a high piezoelectric coefficient. Furthermore, it can store large amounts of energy due to its high energy density and operates over a wide range of temperatures, making it functional in many locations. However, PZT is brittle, which makes it susceptible to mechanical failure [10], and its lead composition raises environmental concerns.

PVDF is a flexible polymer, making it suitable for integration into systems that require various shapes and sizes, along with being resistant to mechanical stress and environmental factors [11]. Although, because of its lower piezoelectric coefficient, it generates less electrical energy when compared to PZT. Furthermore, it is unable to store as much energy as PZT material due to its lower energy density.

Piezoelectric composites are materials designed in recent years to address the limitations presented by PZT and PVDF. Piezoelectric composites allow the combination of the properties of ceramics and polymers by embedding piezoelectric ceramic elements in a polymer matrix, hence making them suitable for various applications [12]. These materials are more flexible and durable than PZT and have a piezoelectric coefficient that varies between the piezoelectric coefficients of PZT and PVDF. There is a large variety of these piezoelectric composite materials, all with different specifications, meaning that a material should be selected based on the factors of the given situation.

2.2.3 Energy Conversion Process

The general process for how mechanical stress generates energy via the utilisation of the piezoelectric effect is outlined in Piezoelectric Energy Harvesters. In general, the electrical output from piezoelectric materials outputs an alternating current, which is often rectified to become a direct current for application. There are core equations that represent both the power output and voltage of a given piezoelectric system. The power output is dependent on the capacitance of the piezoelectric material, the voltage generated, and the frequency of the mechanical vibration, calculated using the equation (1).

$$P = \frac{1}{2} \times C \times V^2 \times f \quad (1)$$

Furthermore, the voltage of the piezoelectric material is determined by the force applied to the material, the area of the piezoelectric material, and finally, the piezoelectric coefficient given by d_{31} as given in the equation (2).

$$V = d_{31} \times \frac{F}{Ar} \quad (2)$$

As seen in both equations (1) and (2), the output of a piezoelectric system is strongly dependent on the properties of the piezoelectric material as well as the characteristics of the forces acting on it.

2.3 Vortex-Induced Vibrations

2.3.1 Vortex-Induced Vibrations and Karmen Vortex Streets

Vortex-induced vibrations occur when fluids flow past a bluff body, generating alternating vortices on either side of the body, as demonstrated in Figure 3. The frequency of underwater currents is extremely low, typically ranging from 0.001 to 0.03 Hz, making them highly ineffective with the use of PEHs unless they are manipulated. Equation (1) demonstrates this outcome as a low frequency leads to low power output.

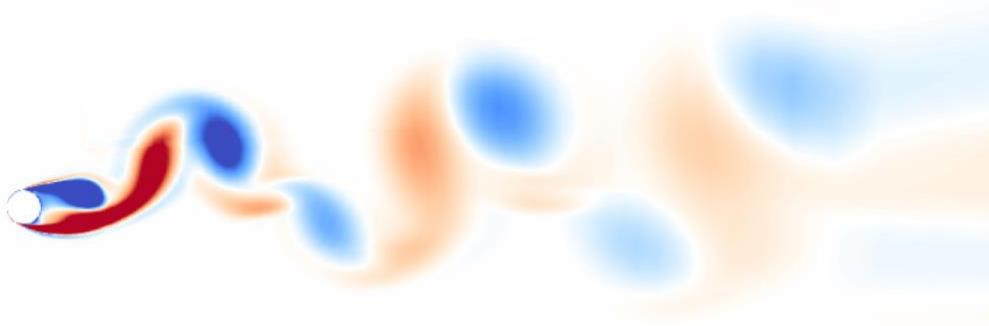


Figure 3 - Diagram of Vortices Produced by VIV of a Circular Cross-section Bluff Body [13]

This allows a periodic force with a higher frequency to act on the generator, thereby providing a means to harvest energy from such a low-frequency force through the implementation of a piezoelectric energy harvester. Vortex-induced vibrations are influenced by several key factors, including the velocity of the fluid, the shape of the bluff body, fluid viscosity, and submergence depth. These factors can be characterised using the Reynolds number, which is a dimensionless quantity used to predict the flow pattern and behaviour of the fluid represented in equation (3).

$$Re = \frac{\rho u L}{\mu} \quad (3)$$

The relationship between the Reynolds number and VIV is demonstrated in [14] as it establishes that the amplitude ratio (A/D) is initially directly proportional to the Reynolds number of a system, it further concludes that there is a

strong dependence between the VIV response and the Reynolds number of the fluid. [14] compares the resulting amplitude ratio as the Reynolds number is increased using a horizontally mounted cylinder, with the results highlighting that at first, when the Reynolds number is increased, the Amplitude ratio rises until it becomes too high, at which point the Amplitude ratio steeply drops off. This demonstrates that there is an ideal Reynolds number that causes the highest Amplitude ratio in vibrations; however, if the Reynolds number is increased too high, it then becomes suboptimal. This same result is concluded in [15], with it instead reducing the Reynolds number by lowering the water's incoming flow rate. Through this method, it was again concluded that a decrease in the Reynolds number correlates with a reduction in the amplitude ratio. [15] does well in concluding that the same result occurs for a lower variation of Reynolds numbers.

2.3.2 *Bluff Body Shapes/Effects of Blockage Ratio on VIV*

For energy harvesting using PEHs, vortex shedding should be increased to maximise the power harvested by the system. Vortex shedding through a confined space is influenced by the blockage ratio (β) of the system, with wall confinement altering both the vortex shedding pattern and wake development [16]. An increase in blockage ratio leads to vortex shedding being completely inhibited and the wake flow becoming steady at high values of blockage ratio, which would have a negative implication on a PEH, although for lower values it is confirmed that vortex shedding is strengthened for the case of blockage ratio increasing from 0.25 to 0.33 [16]. It is also demonstrated that the transition of wake flow from the unsteady vortex shedding state to the steady state depends on the shape of the bluff body, with the circular cylinder bluff body design being the least affected/taking the longest to be affected by the blockage ratio of the system [16]. The report employs a 2D top-down analysis of the various bluff body shapes, concluding that a circular cross-sectioned bluff body would be more effective in generating VIV through vortex shedding than rectangular/square cross-sectioned bluff bodies.

2.3.3 *Effect of Submergence Depth on VIV*

The proximity of the device to the free surface of the water has a negative influence on vortex shedding via the use of a spring-mounted circular cylinder [17]. The paper highlights that the amplitude of the VIV will be gradually suppressed as the submergence depth decreases; however, the paper does not test at submergence depths greater than 0.6 m for water flow rates ranging from 0.3 m/s to 1.05 m/s. When this submergence depth is greater than 0.5 m, the VIV amplitude no longer increases, hence meaning that the effects of the surface of the water or submergence depth can be ignored when the depth of the water is greater than 0.5 m [17].

2.4 Piezoelectric Energy Harvester Designs

2.4.1 Low Speed PEHs

Harvesting energy using PEHs in low-flow-rate systems, while still possible, presents a challenge due to slower flow rates generally not inducing as high a VIV amplitude as those of higher flow-rate systems. The effectiveness of a PEH in these slower flow rate systems is demonstrated in the results of [18], with the PEH in this system still producing the maximum voltage output of 555 mV at a low flow rate of 0.1 m/s . [19] presents a magnetically coupled design as shown in Figure 4, which is adaptable for varying flow rate PEH systems. The design of this PEH allows the magnets to be adjusted to attract or repel, depending on the system's flow rate. For slower flow rate systems, the attractive force of the magnet increased the overall output voltages for D at 28 mm and D at 36 mm increased by 1121% and 61% respectively, when compared to a baseline non-magnetic PEH using the same setup at a constant flow rate of 0.2 m/s [19]. Therefore, a repulsive force acting to move the PEH away from its usual stable position in slower flow rate PEHs can be noted as being an effective way to increase the voltage output of a PEH system.

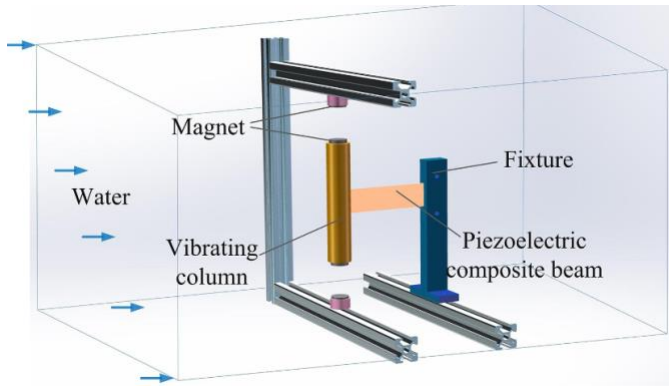


Figure 4 – Diagram of Magnetically Coupled PEH with Cantilever Beam [19]

2.4.2 PEHs Harvesting through a Single Flow

[18] implements and tests a PEH which involves hanging a bluff body connected to a piezoelectric plate into a water flow, with the PEH oscillating due to the vortices induced as the laminar water flow passes by. This experimental setup is similar to [20] and [21], as the water flow is specifically only allowed to flow through the system in a single direction. The paper [18], demonstrated that at low flow rates of 0.1 m/s , the maximum voltage output was 555 mV , occurring when using a cylinder of diameter 0.8 cm , and the minimum voltage output was 140 mV for the cylinder of diameter 0.58 cm . This result demonstrates that harvesting energy from a unidirectional flow of water is an effective way to generate power. Furthermore, as outlined in Section 2.4.5, [20] and [21], reiterate this power production, but at high Reynolds numbers ranging from 3000 to 12000, where the power output reached a maximum of $5321.7\text{ }\mu\text{W}$.

Alternatively, a method involving a rotating propeller with its blades hitting a piezoelectric beam to harvest energy from the constant water flow is assessed in [22]. This alternative method does not involve the use of VIV, as the blades provide the variation in pressure on the piezoelectric material to harvest energy. With a maximum power output of 17 mW , it successfully produces more power than harvesting through VIV; however, it only works effectively with a unidirectional flow and is only shown to be effective at a flow rate of 1.2 m/s . Evidence of a similar design involving magnets attached to both the propellers of a wind-based turbine to compress and decompress piezoelectric transducers and harvest energy also emphasises the effectiveness of using propellers to harvest energy, but only harvested an average power of $1217.8\text{ }\mu\text{W}$ at a much higher wind speed of 7 m/s [23]. This paper failed to demonstrate the improvement of turbine-based PEH designs over VIV-based PEH designs in unidirectional flow systems, as it did not compare power outputs for a slower flow rate system.

2.4.3 PEHs with Multiple Degrees of Freedom

Designs of PEH systems that harvest energy from multiple directions have been investigated in recent years. Specifically, the design of a PEH that harvests energy from movement horizontally and vertically is demonstrated in Figure 5, with it utilising two piezoelectric patches placed on either side of the bluff body [24]. Figure 5 demonstrates the deformation that the structure undergoes, from which the piezoelectric patches will in turn harvest energy. Something to note about this design is that, unlike previously discussed designs, the piezoelectric strips deform in response to the body to which they are attached, meaning that a flexible/elastic material is necessary for this design to function correctly.

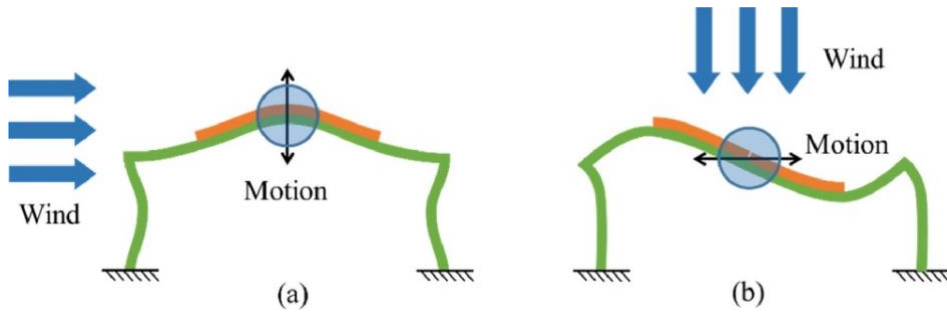


Figure 5 – 2DOF Wind PEH Bending Diagrams [24]

The maximum voltage output of the PEH would also vary depending on the mode that the system was in, as shown in Figure 5. That is, when the system was oscillating in the vertical mode (Figure 5, b) the maximum voltage output would increase with an increase in the length of the side-beam/bluff body. Although if the beam were oscillating in horizontal mode, the maximum output voltage would instead decrease with an increase in side-beam/bluff body length [24]. Furthermore, unlike oscillation in the vertical mode, the wind speed at which the horizontal modes (Figure 5, a) maximum output voltage would occur also decreased with an increase in bluff body length [24].

Overall, it should be noted that the maximum voltage produced in such a system never exceeds 2 V, regardless of the experimental conditions tested. Consequently, the design should be considered worse when compared to the power/voltage output of single-directional flow systems, even though it does provide the ability to harvest energy bi-directionally.

A similar design to paper [24] is also explored in [25], with it incorporating the use of magnets to increase the power output of the system, as shown in Figure 6. The modes in which energy could be harvested remained similar to those of Figure 5. The incorporation of the magnetic attraction within the design allowed the voltage harvested by the PEH to increase from a previous maximum of 2 V [24] to a new maximum of 16 V [25], when energy is harvested in the vertical mode. However, the new design only provides a slight increase of roughly 2 V to the output of the horizontal mode.

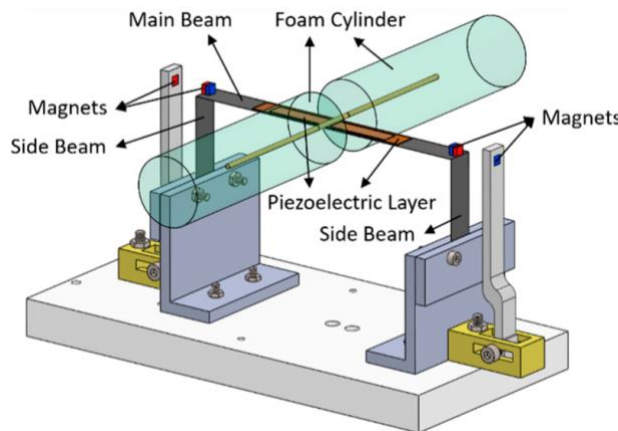


Figure 6 – 2DOF Wind PEH with the Addition of a Magnet [25]

Something important to note from both papers [24] and [25], is that for tests involving low flow velocities, the maximum voltage output remained at approximately 0 V, making it unsuitable for low flow rate systems such as oceanic tides. However, the effectiveness of magnets and the bi-directional energy harvesting capabilities of the design should still be noted.

Generally, in the previously reviewed papers, the piezoelectric devices have been bent due to VIV, hence allowing the PEH to harvest energy. More commonly, PEH systems not involving VIV harvest energy by applying a force to the piezoelectric material, thereby compressing or decompressing the device. This idea is presented in [26], with it featuring a piezoelectric circular ceramic disc placed at sea level, which would compress and decompress as the waves impact with the piezoelectric plate, thereby harvesting energy.

This idea of impact harvesting can then be converted for underwater energy harvesters using a pendulum to impact the piezoelectric strips, as demonstrated in Figure 7 [27]. The results of testing this device concluded that, on

average, $2.2 \pm 0.3 \mu W$ of power were harvested over a 45-minute interval. It is worth noting that the designed device was programmed to activate every three minutes, outputting 3.3 V. In the case where there was enough energy in the battery when activation occurred, the output would be activated and discharged over the load until its voltage started to decrease [27]. Therefore, the electrical circuit presented in this solution may also be helpful for intermittently powering beacons, even though it is currently only being used as a method of measuring system output and logging data.

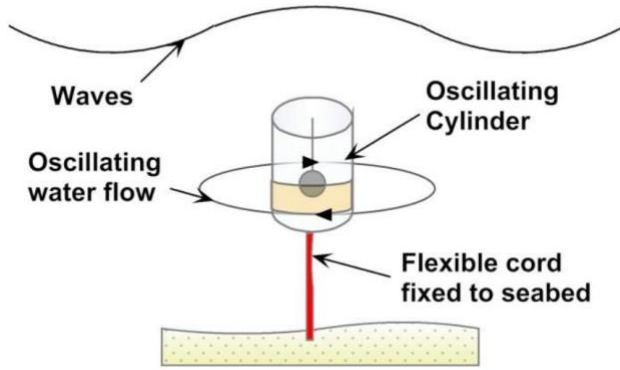


Figure 7 – Impacting Pendulum PEH Diagram [27]

The introduction of a bluff body into this design could make use of underwater currents, as it would assist in generating VIV [28]. This concept is demonstrated in Figure 8, with the article only presenting an idea rather than any experimental or calculated evidence that could demonstrate the overall power output such a system may induce.

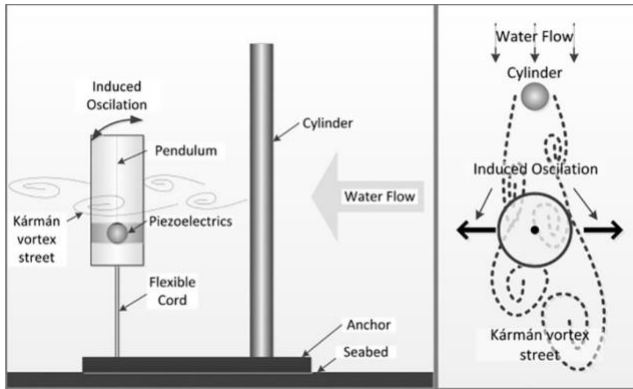


Figure 8 – Impacting Pendulum PEH from the VIV Diagram [28]

Overall, the ideas presented by the design of the PEH in both [27] and [28], demonstrate a solution that would act effectively regardless of the direction of water flow. Although, as shown in Figure 8, the number of bluff bodies would need to be increased such that water / current flow in more directions would still induce VIV, which acts on the PEH to generate power optimally.

This idea of a centralised PEH is again explored in [29], with it instead using a MEMS PEH to harvest energy from wind flow. Figure 9 demonstrates the MEMS PEH's modes of deformation in its piezoelectric material, with the material lying flat, parallel to the plane from which it harvests energy. These modes of deformation enable the centralised PEH to harvest energy regardless of the direction of fluid flow. More details on how this is relevant to bluff body positioning and power output of the device are explored in Section 2.4.4 of this report.

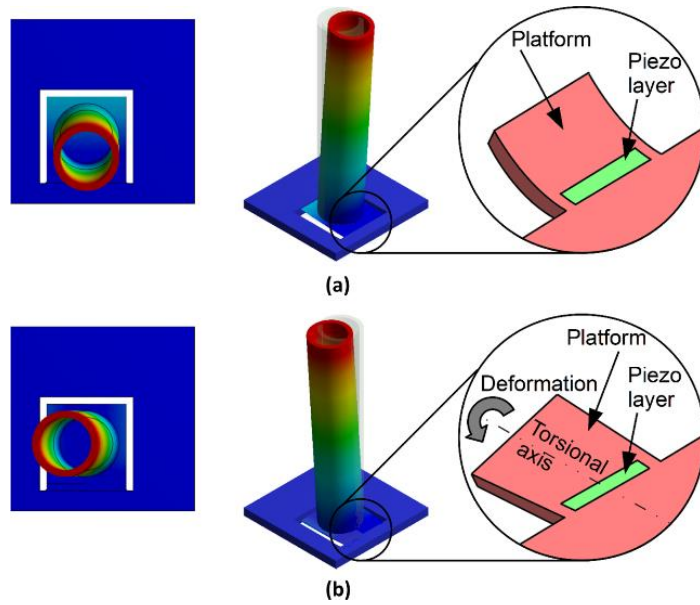


Figure 9 – MEMS PEH Design with Two Forms of Deformation [29]

While the design presented in [29] is not directly applicable to the criteria of this thesis due to its small scale, it does present a unique method of deforming piezoelectric material to harvest energy for flows along an entire plane.

The design presented in the research paper [30] achieves a similar outcome to [29] in harvesting energy from any flow in a singular plane by implementing a cross-coupled piezoelectric design which utilises two single DOF piezoelectric strips attached perpendicularly, with the bottom one also being connected to a bluff body, as shown in Figure 10. It is demonstrated that the power output of each strip varies drastically depending on which strip is parallel to the wind flow. That is, if the upper beam is parallel to the wind flow (Figure 10, Case A), the upper beam generated a voltage maximum of 6 V, while the lower beam did not generate a voltage at a wind speed of 1.0 m/s, noting that this voltage dropped off steeply for wind speeds greater than 1.0 m/s. Furthermore, if the lower beam is parallel to the wind flow (Figure 10, Case B), the results are inverted, with the lower beam generating a maximum voltage of 12 V and the upper beam generating no voltage at a wind speed of approximately 2.75 m/s. Again, noting that the output voltage decreases significantly with an increase in wind speed from 2.75 m/s.

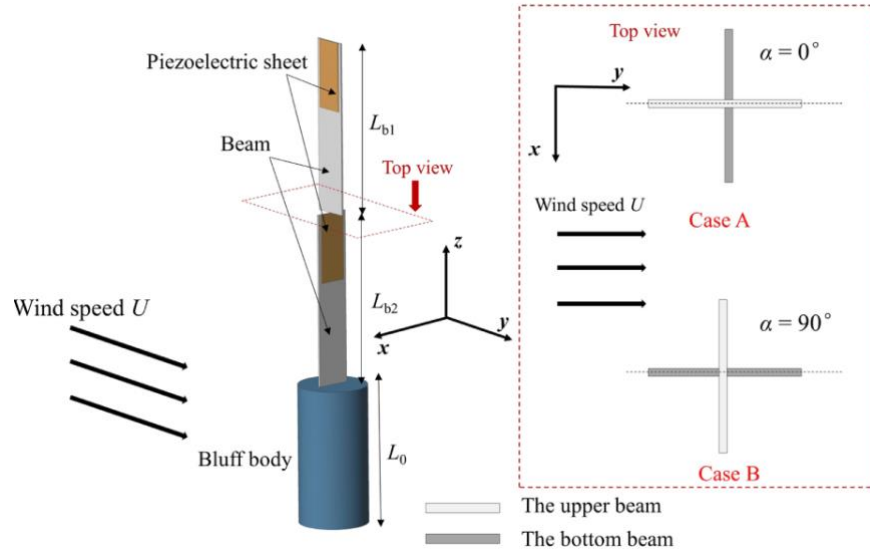


Figure 10 - Two-directional Wind-based Cantilever PEH [30]

However, this paper does not test the energy outputs of wind passing at different angles by the bluff body to determine its effectiveness from a multitude of directions, as it only tests when the wind is acting directly perpendicular to either of the piezoelectric sheets, as denoted in Figure 10 as Case A and Case B. Again, [30] achieves the same number of modes of deformation as found in [29], but on a larger scale, resulting in a larger power output.

Previous papers focused on how the bluff body/design of the system on which the piezoelectric strips sat could be altered to increase the energy output and allow energy to be harvested in multiple directions. Alternatively, the piezoelectric strips' shape can instead be modified to harvest energy in 2DOF [31]. The energy outputs of both U-shape, H-shape, and folded are analysed and compared with the energy harvested from a single DOF system. Simulations conclude that the electrical energy harvested from the H-shape harvester and single DOF harvester under random vibrations, the H-shape harvester can generate $2.81 \times 10^{-6} J$ electric energy during 20 seconds, which is higher than $4.47 \times 10^{-7} J$ of the S-DOF harvester, as shown in Figure 11 [31]. This is a significant result, as a 2-DOF PEH would allow for energy to be harvested in more directions, while also harvesting more energy in a single direction compared to a single-DOF system.

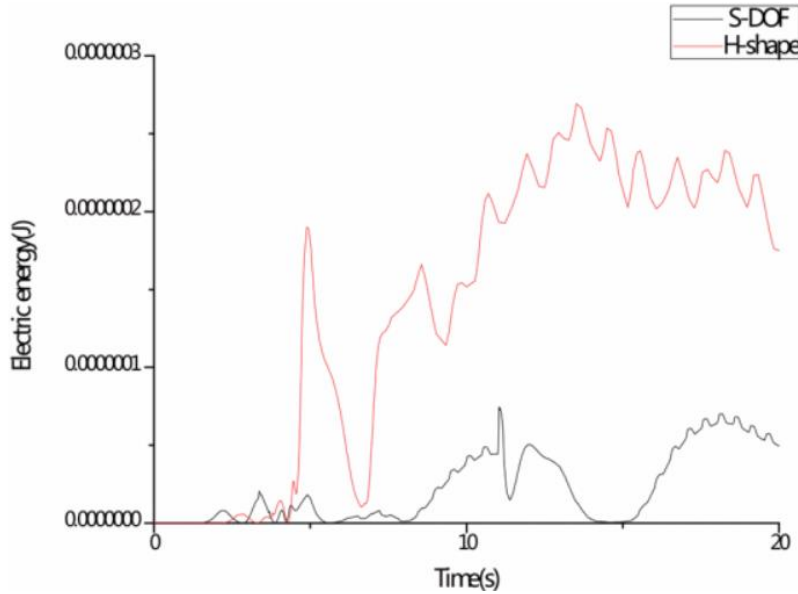


Figure 11 – Graph of Electrical Output Comparison of S-DOF and H-Shape PEH [31]

2.4.4 Positioning of Bluff Bodies Relative to Air Flow and Energy Harvesters

The optimal distance for a bluff body relative to the PEH increases with an increase in fluid velocity [32]. The paper proposed a theoretical model that could be used to determine the optimal distance between the bluff body and the energy harvester, resulting in the highest energy output for a given fluid velocity.

The computational and experimental results highlighted the maximum power and voltage output in relation to the ratio d/D , where d is the distance between the bluff body and the PEH. As shown in Figure 12, the ratio of d/D , which gave the maximum power output in return, increased as the velocity of the fluid increased, ranging from 0.2 to 2.25 [32].

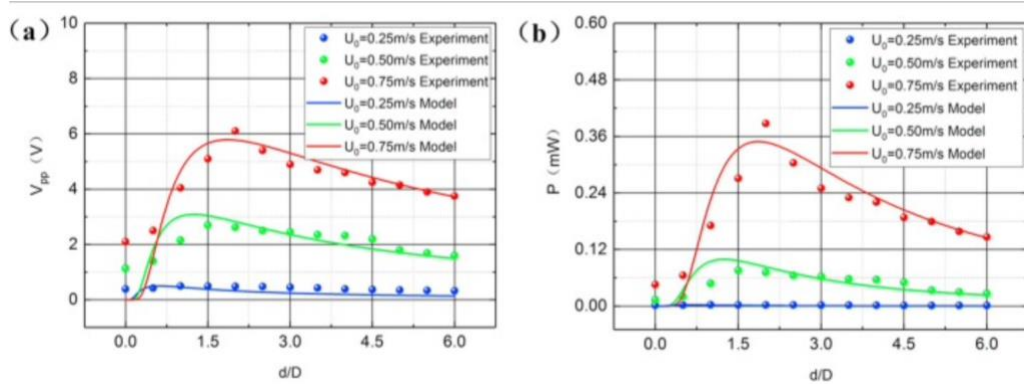


Figure 12 – (a) Graph Representing Voltage Output at Different Distance Ratios, (b) Graph Representing Power Output at Different Distance Ratios [32]

Furthermore, [33] implements the use of two consecutive cylindrical PEHs arranged in sequence, with the first acting as a bluff body for the second. This highlighted that the second PEH performed optimally when the spacing between the two harvesters was $2D$, and analysed results for flow rates between 0.1 m/s and 0.7 m/s . Although this paper did not experiment with spacings smaller than $2D$, indicating that a more optimal design involving a smaller spacing could be more effective in harvesting energy through a PEH.

Furthermore, reports involving MEMS PEH devices to harvest energy effectively from wind VIV in a horizontal plane have been explored [29]. The schematic of this design is demonstrated in Figure 13. The report effectively demonstrated that the PEH was more efficient in harvesting energy when surrounded by bluff-body cylinders, as they produce VIV acting on the PEH oscillator at the centre of the MEMS chip. The report considered configurations involving three-by-three, five-by-five, and no bluff bodies at all. Power harvested was optimal during the three-by-three setup of VIV, with it producing $1.6nW$ of power at a flow rate of 5.82 m/s [29].

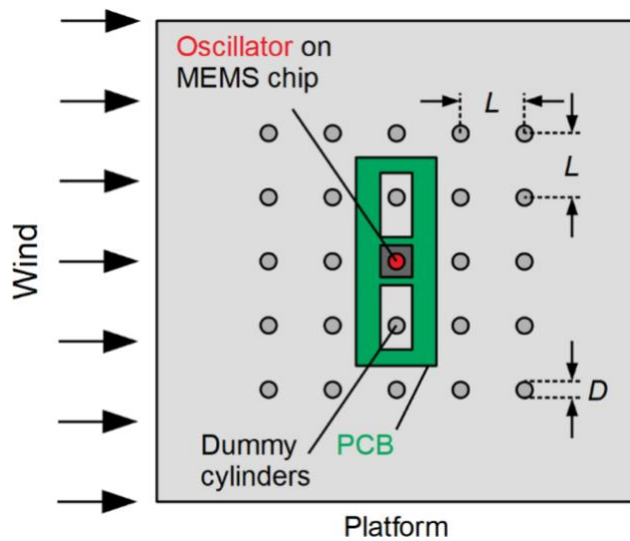


Figure 13 - Schematic Drawing of MEMS PEH [29]

Although the design harvested minimal amounts of energy due to its MEMS nature, the ideas generated regarding surrounding a PEH with bluff bodies demonstrate an effective way to harvest energy, regardless of the direction of fluid flow.

2.4.5 Effects of Bluff Body Shapes/Cross-sections on Piezoelectric Energy Harvesters

Study [20] assists in demonstrating the relationship between bluff body size/shape and the overall power output of a PEH at low Reynolds numbers with a constant flow velocity of 0.26 m/s in water. The comparative analysis of two bluff bodies, one of 25 mm and the other with a diameter of 12.5 mm , results in the 25 mm bluff body causing a 17% increase in the amount of energy harvested [20]. Overall, this paper effectively demonstrates the existence

of a relationship between power output and bluff body size; however, it does not consider the changing shape of the bluff bodies themselves or evaluate a sufficient number of bluff body sizes to determine an optimal one.

Paper [21] uses a PEH system which is set up in a channel/pipe such that water is flowing continuously through it with the PEH hanging from a compartment above, and the bluff body attached to it being oscillated by the water flow, as shown in Figure 14. This paper compares the resultant power output to the Reynolds number/flow rate of the water flow past two bluff bodies, one with a circular cross-section and the other with a U-shaped cross-section. The experimental set-up and U-shape bluff body design are demonstrated in Figure 14.

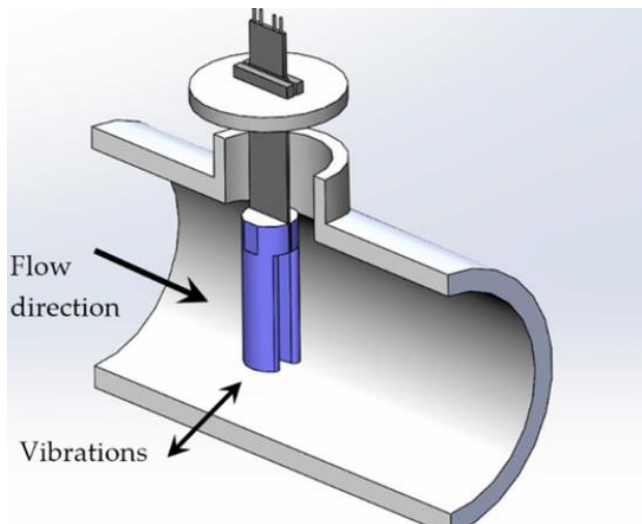


Figure 14- Diagram of U-shaped Bluff Body Setup for PEH in Pipe [21]

It is also shown that the maximum power output for the U-shaped bluff body and cylindrical bluff body were $5321.7 \mu W$ and $1848.3 \mu W$, respectively. Therefore, [21] concludes that the U-shaped bluff body performed considerably better for the maximum tested Reynolds number of 12000. Furthermore, this disparity between power output decreased as the Reynolds number decreased. Still, for bluff bodies with the same length, the U-shaped bluff body outperformed its cylindrical counterpart when the same Reynolds number was applied. A similar result is concluded by [34], which utilises the same experimental testing but only using a cylindrically shaped bluff body, with the maximum power output being $996.25 \mu W$ corresponding to a Reynolds number of 12000. [21] also highlights the effect in which bluff body length has an overall power output, as shown in Figure 15, the cylindrically shaped PEH, with a length of 20 mm, slightly outperforms the U-shaped PEH, with a length of 10 mm, at a higher Reynolds number of 12000. However, for lower Reynolds numbers, the difference in power output is minimal. This demonstrates that the length of the PEH bluff body is an influencing factor for the bluff body when VIV/power output is the intended outcome. Something interesting to note from [21] is that the surface area of the bluff body facing the water flow does not differ from cylindrical to U-shaped bluff bodies, hence implying that the type/strength

of the VIV is not only determined by the surface area that the water flow initially impacts, but also by the back side of the bluff body.

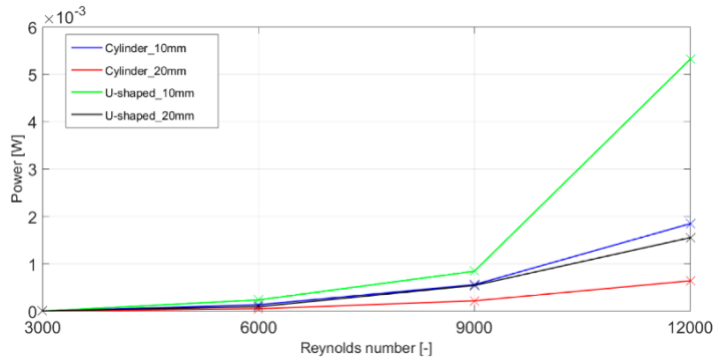


Figure 15 – Graph Comparing the Power Output of Cylindrical-shaped and U-shaped Bluff Bodies at Different Lengths [21]

Both the shape of a bluff body and the flag configuration of the piezoelectric energy harvester are crucial factors that affect the amount of energy harvested by a PEH [35]. Although this paper focuses on wind speed rather than water, the effects of bluff body shape on the amount of energy generated should remain comparable, as both water and wind act in a similar manner, inducing VIVs within the system in which they are implemented. The paper worked on enhancing low-speed wind energy harvesting, similar to that of the low-speed underwater currents in oceans. It concluded that bluff bodies with higher drag coefficients could better excite the longer, fully active piezoelectric flags, resulting in more energy being generated. Although for the same bluff body shapes, shorter flags could generate more energy in higher wind speeds. [35] demonstrates that the ideal length of the flag decreases with the speed of the wind when the aim is to increase the amplitude of the generated voltage. Furthermore, for lower wind speeds, a symmetrical bluff-body design demonstrated in Figure 16 is ideal for harvesting the most energy from the piezoelectric energy harvester [35].

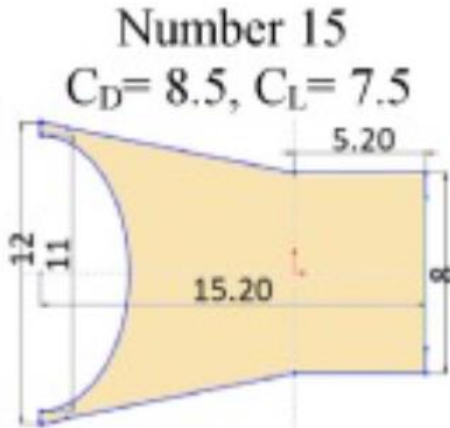


Figure 16 - Diagram of the Most Effective Bluff Body Cross-section Shape from [35]

The previously considered bluff bodies did not involve the consideration of a hybrid bluff body. Hybrid bluff bodies are objects with cross-sections that do not remain constant throughout their entire length. [36] does well in considering the effects of such a body on the output voltage of a wind-based piezo-aeroelastic energy harvester. This paper effectively highlights the impact of bluff bodies, consisting of O-shapes and D-shapes, on the resultant maximum voltage of the energy harvesting system, as shown in Figure 17. The research concludes that having a bluff body with the shape O-D-O-D-O or D-O-D as its cross-sections results in an increased maximum voltage of 41.4% and 38.2% when compared with the classical cylinder alone. Although this paper is not conclusive evidence that a hybrid-based bluff body is better in low flow rate systems, as it only tests the average power output for flow rates of 2.6 m/s and 3.6 m/s , it should still be considered when designing the bluff body for a PEH.

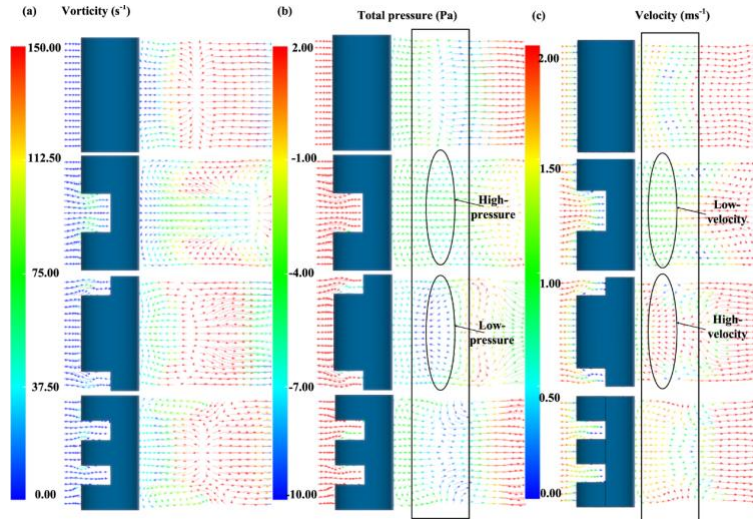


Figure 17 – Diagram Comparing Velocity and Total Pressure Flows of Different Hybrid Bluff bodies [36]

An alternative method to enhance power output for cylindrical PEH systems is to attach two cylindrical rods to the body of the cylinder, facing the direction of the flow rate of the water, as shown in Figure 18 [37]. It is determined that when widening the placement of these rods, the VIV frequency and amplitude are also altered, and hence, the power output of the system also changes [37].

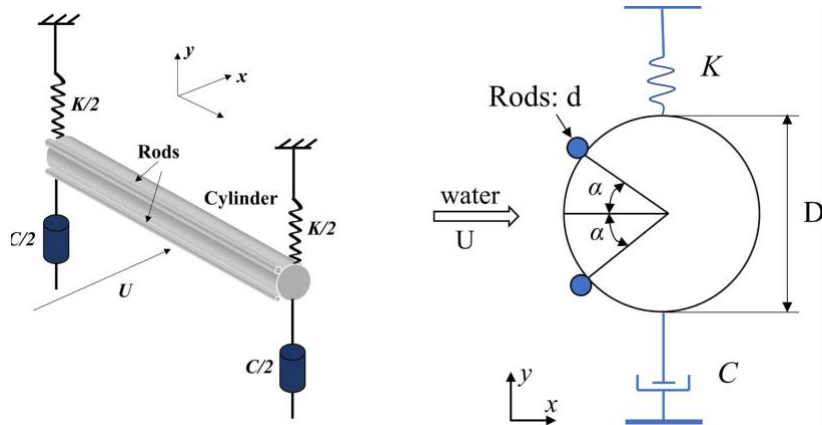


Figure 18 – Experimental Setup of Piezoelectric Energy Harvester and Corresponding Rod Placement Locations [37]

The maximum power output of 2.94 W in this system occurred when the angle of rod placement was 65° with a flow rate of 1.3 m/s . Overall, it should be noted that within the range of rod placement angles from 55° to 65° , better performance on the energy harvesting output and efficiency than that of the bare cylinder occurred, as demonstrated in Figure 19. Although the results of this paper should be more closely related to the properties of the surface area/shape of the bluff body, instead of treating the rod placement on the bluff body as a new factor that affects VIV/energy output of the design.

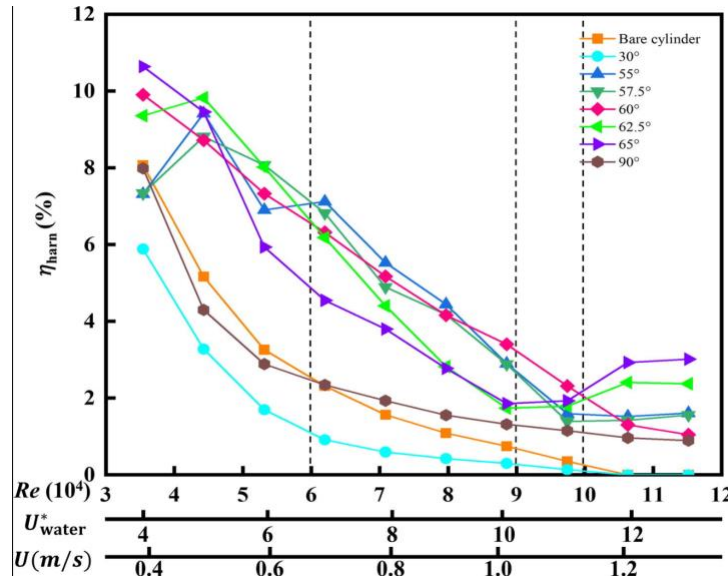


Figure 19 – Graph Comparing Energy Efficiencies with Different Rod Placements to Flow Rate [37]

2.4.6 Single Bluff Body Vs Implementation of a Separate Bluff Body

As stated previously, the paper [33] compares the power output of dual cylindrical PEHs arranged in sequence, where the first PEH acts as a bluff body for the second, with the power output of a single PEH alone. Table 1 highlights the results of the paper with DPEH-151-1 representing the first PEH and DPEH-151-2 representing the second PEH in the dual PEH system, while SPEH-151 represents the single PEH acting alone. Table 1 demonstrates that if the resultant maximum voltage for each situation is compared, ignoring the voltage output of the first PEH in the dual system, the PEHs in the dual system produce a significantly greater maximum output voltage compared to the single PEH, which does not have a bluff body upstream to generate any vortex shedding. That is, the voltage output is 199% and 118% of the single PEH voltage output [33] for the second PEH in the case where the spacing distances are $2D$ and $6D$, respectively. Even though the resultant increase in overall maximum voltage is reduced when the distance between the two consecutive PEHs increases, the increase should still be noted as being caused by the vortex shedding of the first PEH in the stream acting as a bluff body. This significant difference can hence highlight the effectiveness of using bluff bodies in PEH systems.

Table 1 - Comparing Maximum Voltages for Different SDOF and 2 SDOF PEH Systems [33]

Name	DPEH-151-1	DPEH-151-2	DPEH-151-1	DPEH-151-2	SPEH-151
Spacing distance W(mm)	2D	2D	6D	6D	-
Maximum RMS Voc (V)	14.63	27.65	15.29	16.34	13.88
Ratio with the SPEH	105%	199%	110%	118%	100%

2.5 Concluded Gaps in Literature

Key gaps in the literature focus on the limited development of effective non-MEMS cantilever-based PEH devices, which are compact in height. Conventional designs are often vertically extended due to the serial mounting of the bluff body with the piezoelectric cantilever, resulting in tall structures that are unsuitable for applications where space is constrained, such as the integration of such a device with an ROV. Additionally, literature highlights the importance and effectiveness of sequential PEH configurations, which in some cases have been shown to double the power output compared to a single PEH system [33].

Furthermore, although MEMS-type PEH devices, which mount the cantilever and bluff body perpendicularly to conserve space, such as that discussed in [29] show promise, no scaled-up versions have been developed to account for the higher energy requirements. Additionally, many of these devices are designed to operate through wind-based excitation instead of through underwater current flow, with the dynamics of the situation differing significantly.

3 Methodology

The overall methodology of this report is based on four main milestones. Milestone one involves determining a PEH design and recreating the experimental results through virtual simulations, Milestone two relates to the design and testing of a singular PEH similar to that of the study completed in Milestone one but with adjustments and improvements made such that it becomes suitable for the desired use case, Milestone three takes the single PEH designed in Milestone two and tests it in a multi-PEH setting, and finally Milestone four works on the design and testing of a shell for the PEH which can be attached to the BlueROV2. These general milestones are visually demonstrated in the flow chart of Figure 1.

3.1 M1 - Validation of Simulation Accuracy and Previous Report Analysis

To validate future simulation results of a final PEH design, it was necessary first to analyse and recreate existing experimental results of a similar PEH. This process involved several steps, including identifying possible improvements to the existing design. These steps are outlined as follows.

3.1.1 Selection of PEH Design Type

To develop a valid PEH design, it is first required to determine the limitations of the parameters of possible designs. Specifically, the initial limitations are determined by the dimensions and size of the BlueROV2 device, with the goal being that any implemented PEH would have a minimal impact on the motion and control of the ROV. The height of the BlueROV2, for which the device is designed, sits at 253.9 mm. To minimise the impact of the device on the ROV's movement, the height of the final design should be limited to 100 mm. Thus, the combined height of each bluff body and piezoelectric material should be approximately 90 mm to allow sufficient headspace for potential modifications aimed at minimising drag.

3.1.2 Mode Shape and Natural Frequency Extraction Process

After a valid PEH design has been selected, the natural frequencies and mode shapes of an already existing similar PEH device should be validated by comparing already existing experimental results with simulation results. To achieve this, computer-aided design (CAD) models of the previous experimental PEH should first be created, and the experimental conditions, such as flow type and flow rate, should be established. Once these experimental factors have been established, complex simulations can be created using the ANSYS Workbench software to recreate the natural frequency results. Inside the ANSYS Workbench, three sub-software programs are used sequentially to determine the natural frequencies of the results: ANSYS Fluent, Static Structural, and Modal. Fluent is first utilised to determine the pressures acting on the PEH body, implementing experimental conditions related to flow type and flow rate. This fluent pressure data is then passed to the static structural analysis, which applies the loads and boundary conditions to determine the stresses and deformations, which are then used as prestress inputs for the

modal analysis. This modal analysis then outputs the structure's natural frequencies and mode shapes, which can then be compared to the experimental results of the selected existing report.

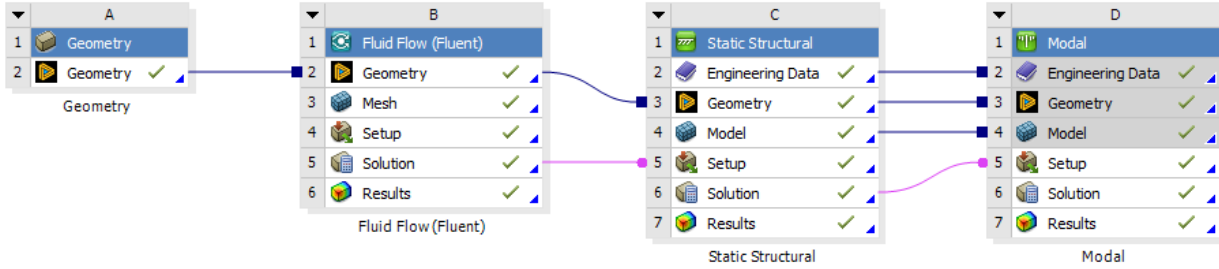


Figure 20 - ANSYS Workbench Simulation Setup for Natural Frequencies and Mode Shapes

This entire process is outlined in Figure 21, highlighting how the solutions of fluent and static structural analyses are passed to the setup portion of static structural and modal analysis, respectively. If the simulation outputs natural frequencies and mode shapes that align with those of the experimental results, the outlined simulation process can be considered correct and can be implemented in future simulations for a newly created PEH design.

3.1.3 Analysis of Existing Design Vortex Shedding Frequencies

To analyse the overall effectiveness of the previously implemented design and establish any possible improvements or aims for future designs, the vortex shedding frequency induced by the bluff body needs to be determined. As VIV frequency remains relatively independent of the height of a bluff body, with it depending mainly on the cross-sectional shape, a 2D analysis of the bluff body's cross-section needs to be completed. This process involves the use of ANSYS Fluent, where a 2D CAD sketch representing the cross-sectional profile of the bluff body is first created and imported into the Fluent simulation environment shown in Figure 21.



Figure 21 - Example 2D CAD Sketch Representing the Cross-sectional Area of the Bluff Body

A fluid flow is then simulated across this cross-section, replicating experimental conditions such as velocity and pressure. The simulation then extracts the transient lift force generated due to vortex shedding over the cross-sectional shape, with an example shown in Figure 22 (a). This lift force is then plotted with respect to time, which

then allows the use of ANSYS Fourier transformation to analyse the frequency of the VIV, shown in Figure 22 (b), with the VIV frequency determined as the frequency at which the maximum magnitude occurs.

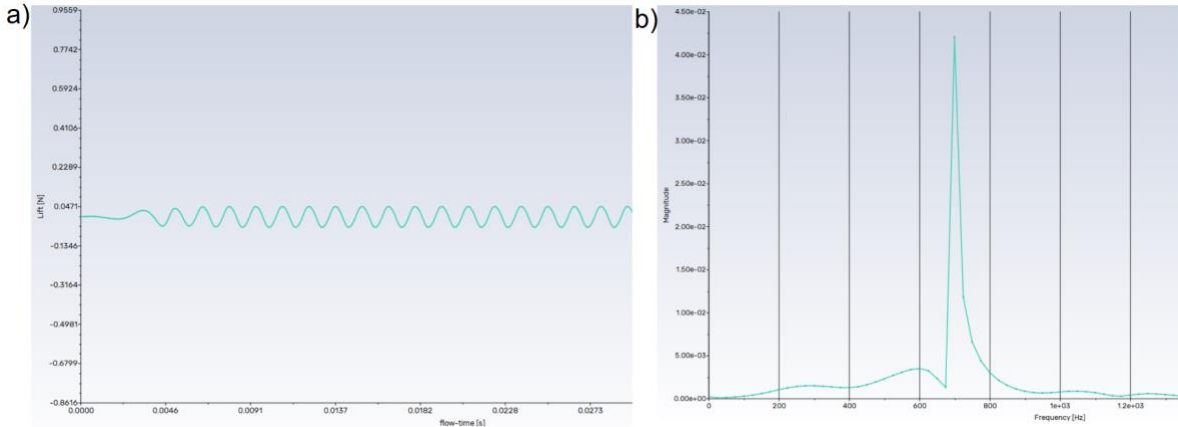


Figure 22 – a) Example Lift Force Vs Time Graph on Bluff Body Cross-section b) Fourier Transformation of Lift force vs Time

This resultant VIV frequency is then compared to the established natural frequencies of the already existing PEH device, as significant discrepancies between VIV frequencies and natural frequencies can lead to non-optimal or reduced energy harvesting efficiencies. This is due to little or no resonance occurring in the device, resulting in lower induced stresses and strains in the piezoelectric material and, consequently, reduced electrical output.

A two-way coupled simulation using ANSYS Fluent and Transient Structural is also necessary to analyse the VIV induced by the bluff body. This two-way coupled simulation setup is represented in Figure 23, with it utilising the previously created CAD model for the existing PEH. The simulation allows for bidirectional interaction between ANSYS Fluent and Transient Structural, where the fluid flow applies pressure forces to the structure, and the resulting structural deformation feeds back to influence the fluid domain in real time.

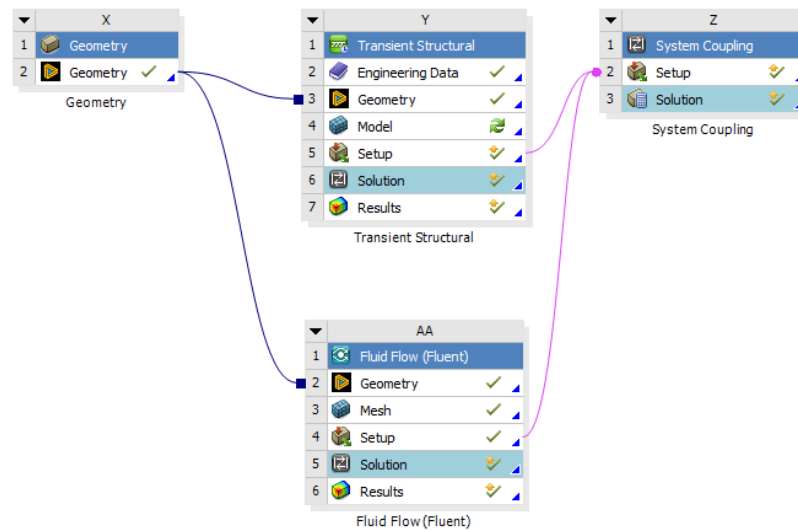


Figure 23 – ANSYS Workbench Two-way Coupled Simulation Setup

Once this simulation has been completed, the overall contours can be created from the provided ANSYS Fluent results, allowing the visual analysis of any vortices. Again, if the structure's natural frequencies differ significantly from those of the VIV frequencies, resonance will be weak or absent, leading to reduced energy harvesting performance. Additionally, if the flow rate is too high for the current structural configuration, VIV may not occur at all. This is due to the VIV frequency being dependent on the Reynolds number, which varies with the fluid's flow rate. This situation will be apparent in any contours, as vortices will again be minimal or completely absent.

3.1.4 Setup for Power Output Simulation

Finally, the power output of the determined PEH can then be recreated via the use of ANSYS simulations. The flow rate at which the peak power output of the experimental device occurred should be examined via the use of the same two-way coupled simulation setup used to analyse the vortices induced by the structure in Figure 23. Using the Transient Structural simulation results, the voltage of the design can then be estimated over the duration of the simulation using equation (4), derived from the Piezoelectric Constitutive equations [38].

$$V = \frac{E \cdot t}{\epsilon_{33}^T} \cdot (d_{31} \cdot \epsilon_x + d_{31} \cdot \epsilon_z + d_{33} \cdot \epsilon_y) \quad (4)$$

Where t is the thickness of the material in metres, d represents values from the piezoelectric coupling matrix in m/V, ϵ represents the mechanical strain tensor, E represents Young's modulus, and ϵ_{33}^T represents the permittivity in the poling direction. This formula should be applied to the top surface of the piezoelectric material, allowing for the average voltage across it to be extracted. Once the voltage has been determined, equation (5) should then be implemented to calculate the overall average power output of the system. This analysis should be completed using a Python script.

$$P_{avg} = \frac{1}{T} \int_0^T \frac{V(t)^2}{R} dt \quad (5)$$

This power output should be consistent with the experimental results reported in the previous PEH study, validating the accuracy of future simulation results used in the design of the new PEH.

3.2 M2 - Design and Simulation of Single-PEH

Milestone two involves the design and simulation of a single-PEH device. The design of this device will initially include the creation of a CAD model, taking into account its dimensions and size. The design of this single-PEH device will be similar to that of the previous PEH study, such that the results of any simulations will be considered reliable and accurate. Analysis of the vortices that the bluff body induces will be completed in this milestone to form an optimal design. The final analysis in this milestone will involve simulating the power output of the single PEH designs. The single PEH design, which is determined to have the most optimal power output, will then be used in the design of the multi-PEH system discussed in Section 3.3.

3.2.1 Dimension and Sizing Considerations

As mentioned in Section 3.1.1, the height of the BlueRov2, for which the device is designed, sits at 253.9 mm, meaning the overall height of a single PEH device will be limited to 100 mm. The similar PEH from a previous study must be modified to accommodate the new environment, specifically, the newly designed PEH needs to be able to effectively harvest power in near-shore underwater environments where these ROVs are most commonly used, which have flow velocities ranging from approximately 0.1 – 0.5 m/s [39]. Other factors, such as the design requiring effective energy harvesting, regardless of water flow direction, must also be considered when selecting a bluff body cross-sectional profile, as well as in overall PEH design.

3.2.2 Bluff Body Vortex Frequency Measurements and Material Selection

Through research, an initial bluff body cross-sectional profile shape can first be determined along with suitable materials for the given design requirements. Since power output testing requires a significant amount of computational power, the number of power output simulations must be limited. To limit this testing, calculations and simpler simulations relating to the VIV frequencies induced by the bluff bodies will first be compared to that of the natural frequencies of each PEH, since to maximize power output of the solution, the natural bending frequency should match that of the VIV frequency generated under the set conditions, such that resonance can be induced.

This initial testing will require two main steps, the first of which is to conduct hand calculations for the vortex frequencies across each bluff body cross-sectional profile using equation (6).

$$f_v = \frac{St \cdot u}{D} \quad (6)$$

Where St is the Strouhal number of the cross-section, u is the fluid velocity, and D is the diameter of the body. Then, to validate these calculations, more advanced CFD simulations will be implemented to confirm these results for each bluff body cross-sectional area. These simulations are the same as those conducted and discussed in Section 3.1.3 of the report represented in Figure 22.

Following this, the simulation methodology, which was previously outlined in Section 3.1.2, is then implemented to evaluate various PEH configurations. In this stage, multiple material combinations and geometries are applied to the PEH's components for analysis. For each design iteration, the natural frequencies are extracted and compared directly to the previously determined VIV frequencies. Through this iterative simulation process, the natural frequency response of each configuration is systematically evaluated with designs that have natural frequencies aligning closest to the induced VIV frequencies being identified as optimal. This approach allows for the selection

of the most effective material pairings for each bluff-body cross-sectional profile, hence determining the designs that will be eventually tested for power output.

3.2.3 Power Output Simulation Under Laminar Flow

The same simulation process as that validated in Section 3.1.4 will be implemented to determine the power output of the design. Design configurations whose natural frequencies most closely match the induced VIV frequency at target flow rates, as identified through the Section 3.2.2, are then selected for power output simulation. Through the methodology of Section 3.1.4, the power output of each PEH at flow rates of 0.1 m/s , 0.3 m/s , and 0.5 m/s will be simulated, along with CFD contours of the vortex shedding induced by each, with an example contour demonstrated in Figure 24. A final single PEH design will then be concluded based on how effectively power is harvested at each flow rate, and then further tested for the multi-PEH design of the system.

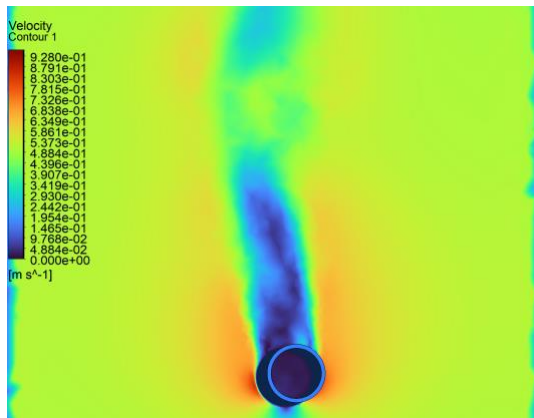


Figure 24 - Example Single PEH Velocity Contour With Cylindrical Bluff Body

3.3 M3 - Design and Simulation of Multi-PEH

Milestone three involves integrating the most effective single PEH design identified in Milestone two into a multi-PEH system for further simulation and testing. Specifically, this section looks at how different separation distances between PEHs impact the power output of a single PEH. This section will conclude an optimal layout for PEHs such that it meets the overall power requirements of the ROV's beacon.

3.3.1 Spacing Strategy and Arrangement Configuration

Research and simulations will again be completed to determine the optimal distance between each PEH's bluff body. The distance between each bluff body will be relative to the bluff body's cross-sectional diameter of each PEH. Since the effectiveness of PEH power output varies significantly depending on the cross-sectional profile, multiple designs will need to be constructed. A CAD model of a three-by-three piezoelectric configuration will need to be made for each different bluff body separation to determine the optimal distance. An example CAD model is demonstrated in Figure 25 showing a cylindrical bluff body separated by a distance of $2D$.

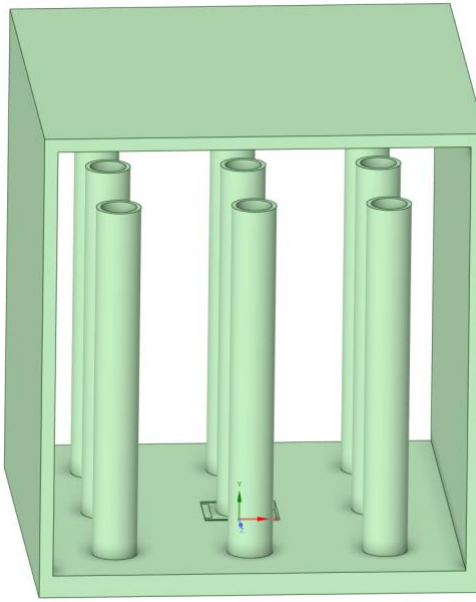


Figure 25 - Example Three-by-Three CAD Model with Separation of 2D

3.3.2 Setup for Multi-Body Coupled Simulations

Again, due to the complexity and significant computational requirements of two-way coupled simulations, only the centre PEH will be set to have a dynamic mesh, meaning that the outer PEHs will remain static and induce a constant VIV. This may affect the reliability and accuracy of results, but it is necessary due to the significant computational power and mesh sophistication required if all PEHs were to act dynamically. The process used for calculating power output will again be the same as that completed in Section 3.1.4 of the report, with the simulation being set up the same as that shown in Figure 23. These simulations will be completed for flow rates of 0.1 m/s , 0.3 m/s , and 0.5 m/s , with both the power output and velocity contours being extracted for results.

From these results, an optimal layout for the multi-PEH setup can then be deciphered to maximise power output. This includes the separation distance, which causes the maximum power output of the centre PEH, as well as the separation distance of PEHs at which the generated VIV dissipates. The distance at which VIV dissipates is essential, as research concludes that the effectiveness of sequential PEHs drops off for the third PEH in a sequence [29], hence separating the PEHs by this distance can act to reset the flow back to its original form and boost power output for the following PEH after the first two.

Furthermore, the power output of the beacon that this system aims to supply power to is approximately 4.17 mW , as calculated in Appendix A. Therefore, the final configuration of PEHs should be such that it meets these power requirements when all PEH powers are summed together.

3.4 M4 - Design and Testing of Multi-PEH Container/Shell

The design and testing of the overall shell design will be conducted in this milestone. This will involve determining general dimensional restrictions such that the device can fit onto a BlueROV2. Furthermore, materials for the shell will be chosen such that they meet all requirements and have minimal effect on the motion of the ROV. This milestone will also conduct a drag analysis on the shell to evaluate the effectiveness of the solution.

3.4.1 Shell Design Considerations for Dimensions and Sizing

The dimensions of the BlueROV2 will be used to determine the overall dimensions of the shell. Specifically, the designed shell will be required to connect to the ROV through the two links with a separation of 340 mm, as demonstrated in Figure 26. Furthermore, the shell can have a length of up to 457.1 mm, which is again the length of the ROV shown in Figure 26. The width can be made wider than 340 mm, but the shell must be designed such that it is fixed to the ROV along these links. The length of the shell can feasibly also be greater than 457.1 mm, but this may not be desirable as it will most likely be unnecessary and possibly inhibit the movement of the ROV.

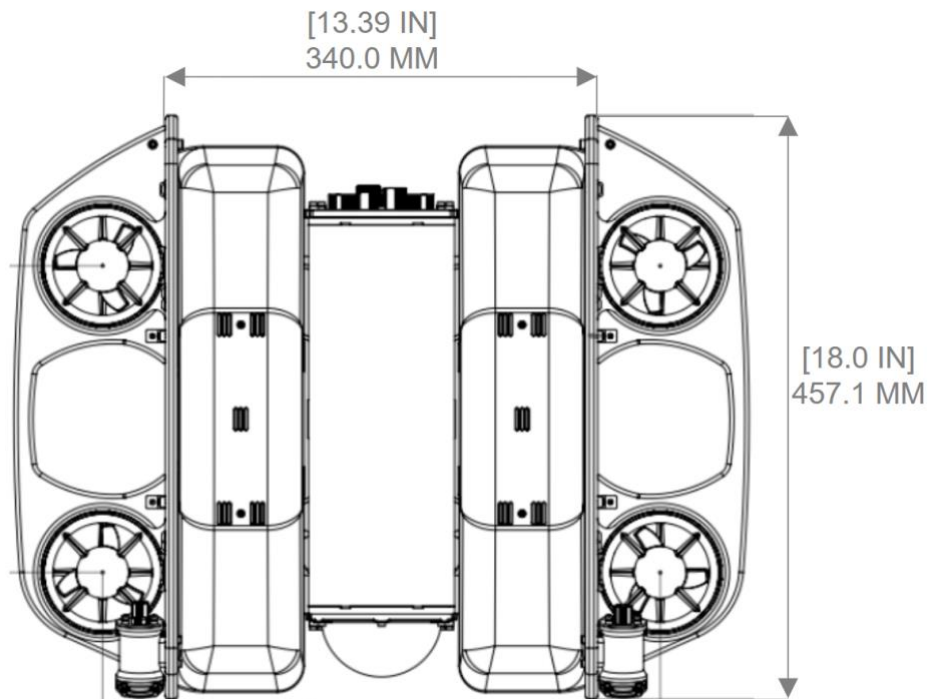


Figure 26 - BlueROV2 Important Dimensions

3.4.2 Shell Material and Shape Considerations

The chosen material for the shell should be determined through research. Specifically, the material must be selected such that the movement of the ROV is minimally impacted. Further factors, including mechanical properties, buoyancy and weight, corrosion and water resistance, environmental conditions, and hydrodynamic performance, must all be researched to determine the optimal shell material.

The physical design of the shell must also be developed, and a corresponding CAD model created. When designing the shell, both weight and drag considerations will be considered to determine a design that minimises the impact on the ROV's motion. Furthermore, since the ROV can move in any direction, the shape of the shell must be such that it minimises the effect it has on drag in all directions. Hydrofoil and streamlined shapes will be analysed, and a suitable design will be developed based on this research. Simulations will be undertaken to determine the drag force induced by this shell with the methodology outlined in Section 3.4.3.

3.4.3 *Simulation Process for Drag Testing of Shell*

To further determine the effectiveness of the shell's design, drag simulations will be completed using ANSYS Fluent. This will involve using Fluent to simulate and acquire the resultant drag force caused by the shell and PEHs for varying flow rates. Since the BlueROV2 can only travel at speeds of up to 1.5 m/s, flow rates of 0.25 m/s, 0.5 m/s, 0.75 m/s, 1.0 m/s, 1.25 m/s, and 1.5 m/s will be analysed.

Once these results have been determined, the drag force caused by the BlueROV2 will then be calculated. Using the drag coefficients found experimentally in [40] along with equation (7) derived in [41], the overall drag in the forward X direction can be determined. This equation uses both the linear and quadratic drag coefficients to assess the overall drag force in a given direction.

$$F_{ROV\ drag} = X_u u + X_{|u|u} |u|u \quad (7)$$

To compare the effectiveness of the implemented design, the drag force induced by the PEH shell can be converted to a percentage of the ROV's drag. An overall shell that induces a drag force that is less than 10% of the total drag induced by the ROV at each flow rate would be appropriate and considered a successful shell design.

4 Results and discussion

4.1 M1 - Validation of Simulation Accuracy and Previous Report Analysis

4.1.1 Justification for Selected PEH Type

As mentioned in Section 3.1.1, the height of each singular PEH must be limited to approximately 90 mm. One such PEH, which conforms to these height restrictions, is discussed in [29], which implements a bluff body perpendicular to a cantilever beam with the piezoelectric material Aluminium Nitride (AlN) attached as represented in Figure 27.

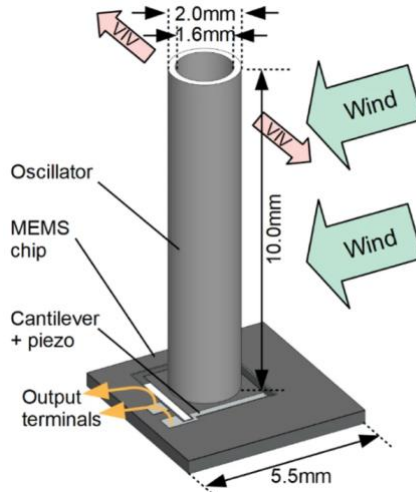


Figure 27 - Perpendicular MEMS PEH [29]

As the bluff body is positioned perpendicularly to the cantilever beam, the resultant height of the design is minimised compared to other beam-type energy harvesting systems, such as that used in [33], where the beam is parallel to the bluff body. Since the device is a MEMS device, the power output is too small for the intended application, so it must be scaled up and modified to meet the new power requirements. Furthermore, the design discussed in [29] was only tested using wind rather than water, so the resultant power output of the device may not be satisfactory. Also, the design incorporates a cylindrical bluff body, enabling the PEH to harvest energy from fluid flows acting in any direction, which is necessary for underwater environments where current flows act in unknown directions. Due to the design conforming to these height restrictions and omnidirectional energy harvesting capabilities, it will be selected as the base design, which future simulation processes will be validated, and will significantly influence the design of the new PEH system.

4.1.2 Validation of Modal Behaviour and Natural Frequencies of Existing Design

To validate the natural frequencies of the design, the previous MEMS PEH in [29], a flow rate of 5.82 m/s was chosen. This was due to the report concluding that the maximum power output of the system was produced at this wind flow rate.

An initial CAD model was first developed, shown in Figure 28 with more details regarding the dimensions of the model located in Appendix B Table 9.

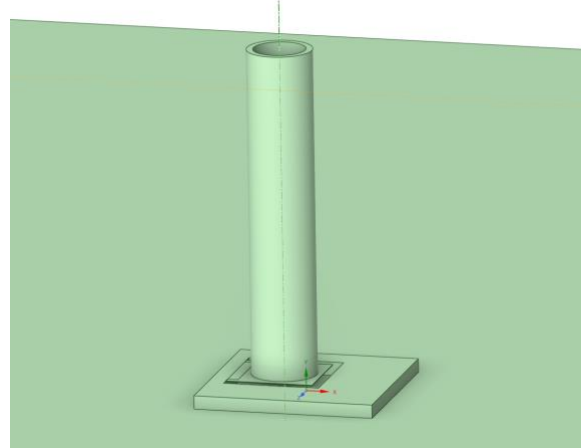


Figure 28 - CAD Model for 2mm Diameter PEH

Utilising this CAD model, the simulation processes described in the methodology of Section 3.1.2 were then completed. The results concluded that a bending moment occurs at 55.28 Hz and a torsional moment at 135.25 Hz , differing by approximately 4.68% and 12.25% respectively from those reported in [29], where it was determined to be 58 Hz and 154 Hz , with these differences justified by the slight variations in the simulation dimensions. Figure 29 and Figure 30 demonstrate these modes of deformation produced from the modal analysis.

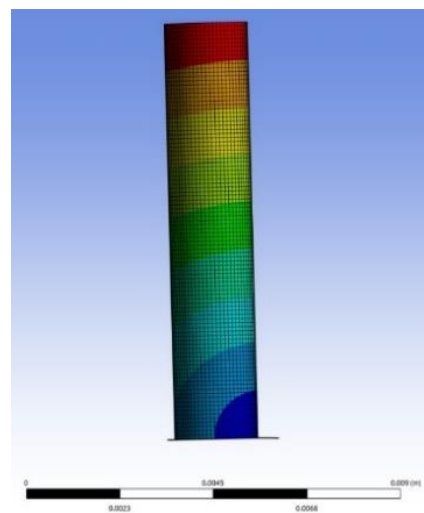


Figure 29 - Bending Mode of Deformation 55.278 Hz

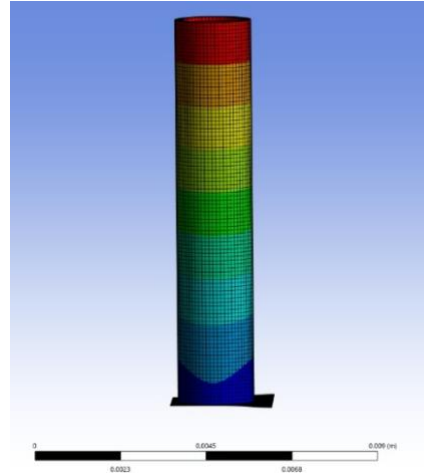


Figure 30 - Torsional Mode of Deformation 135.25 Hz

These results conclude that the simulation procedures conducted successfully validate the previous design for both frequency and modal shapes, as they align closely with the results of [29].

4.1.3 Alignment with Vortex Shedding Frequencies

Analysis of vortex shedding was then conducted, aligning with the methodology outlined in Section 3.1.3. The initial 2D analysis of vortex shedding frequency concludes that a VIV frequency of 699 Hz occurs in these conditions, significantly different from the targeted 55.28 Hz natural frequency at which the system was designed to oscillate. This significant mismatch in frequencies will be considered in future design decisions, as it would mean the system would not harvest power optimally due to the lack of resonance.

The two-way coupled simulation conducted in this section also concluded with a similar result, with it being conducted over a 0.5 second duration, ensuring that the PEH stabilises and begins oscillating under steady state conditions. The velocity flow contour demonstrated in Figure 31 and Figure 32, lacks the presence of VIV as there are no vortices in the flow behind the bluff body in the contour.

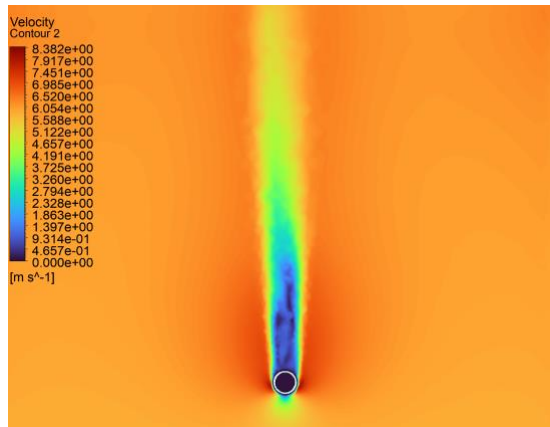


Figure 31 – Two-way Coupled Simulation showing Velocity of Flow Past PEH, Top-down View

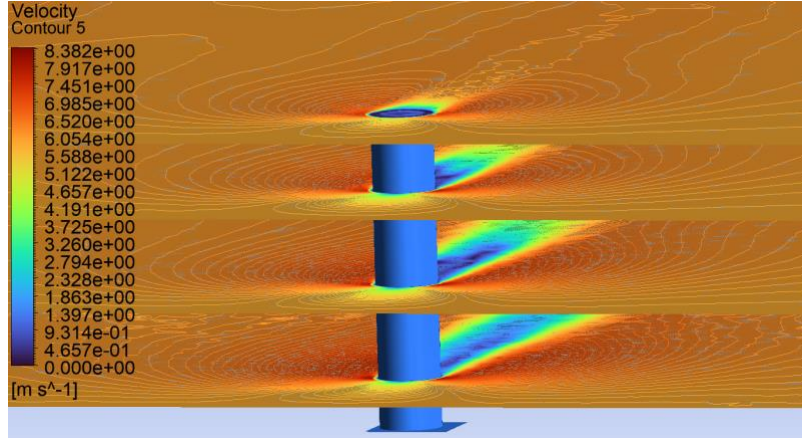


Figure 32 – Two-way Coupled Simulation showing Velocity of Flow Past PEH, Angled View

This lack of VIV aligns with the previously concluded results, which is attributed to a significant mismatch between the vortex shedding frequency generated by the flow and the natural frequency of the PEH design. Results also concluded that under the wind flow of 5.82 m/s , the structure oscillates at an approximate frequency of 53.2 Hz , indicating that the structure oscillated at the desired bending frequency but did not resonate strongly. Since the VIV frequency was significantly higher than the structural frequency, the system likely exhibited only forced vibrations rather than sustained VIV resonance. This mismatch represents a critical design oversight in the PEH configuration presented in [29], and will be a key focus in the development of the scaled-up PEH design.

4.1.4 Simulated Peak Power Performance and Verification

The experimental results of [29] concluded the maximum power output of the system to be approximately 0.8 nW when acting with a wind flow rate of 5.82 m/s , as shown in Figure 33.

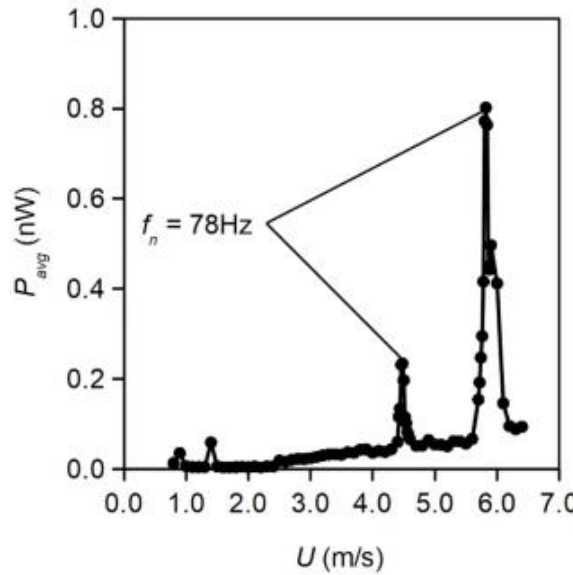


Figure 33 - Power Output vs Flow Rate of MEMS PEH [29]

Using the methodology discussed in Section 3.1.4, the previous two-way coupled simulation of Section 4.1.3, and the piezoelectric properties of AlN listed in [42], the power output was then determined. The results conclude that the average power output over time is approximately 0.4 nW , extracted from the power output vs time graph demonstrated in Figure 34.

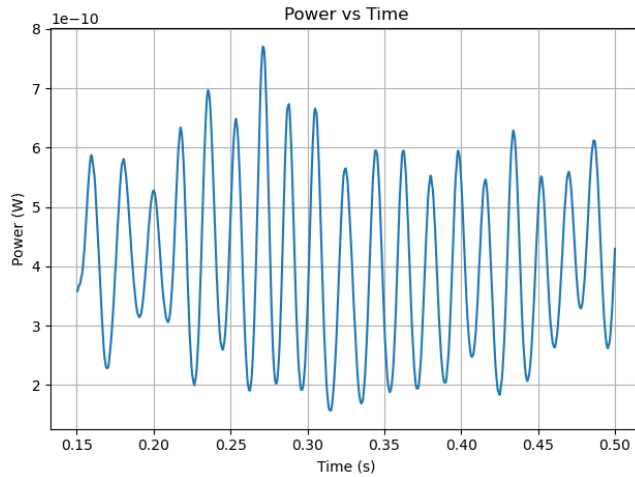


Figure 34 - Power Output vs Time for Simulated MEMS PEH

This result corresponds to 50% of the target 0.8 nW power output experimentally verified in [29]. Due to the sharp nature of the power output peaks, even minor variations in flow rate or geometric parameters, such as those introduced during the device's manufacturing, can significantly shift the location of the peak. This explains why the 0.8 nW peak observed at 5.82 m/s in Figure 33 occurs at a slightly different flow rate compared to that predicted by the simulation. Given that the simulated 0.4 nW output lies just to the left or right of the 0.8 nW peak in the figure, the result can still be considered accurate. Therefore, the simulation approach used to estimate power output is validated and can be confidently applied in evaluating the performance of future PEH designs.

4.2 M2 - Design and Simulation of Single-PEH

4.2.1 Design Decisions regarding Dimensions and Sizing

When designing the PEH for the scaled-up system, the initial geometry and dimensions were generated based on the choice of bluff body diameter. Due to the effectiveness of 10 mm and 15 mm circular cross-sectioned bluff bodies presented in similar systems [33], they were selected for the new single PEH bluff body diameter. The height of the bluff body was increased from 10 mm to 80 mm due to its effectiveness in similar systems such as [33]. Other dimensions were scaled up proportionally by factors of approximately 5 and 7.5 for the 10 mm and 15 mm systems, based on the increase in diameter from the 2 mm examined in [29]. Although in these new models, the thickness of the piezoelectric material was scaled up by a factor of 60 due to the increased power output required.

These dimensions can be found in Appendix B Table 9 with the finalised CAD models for both bluff bodies featured in Figure 35.

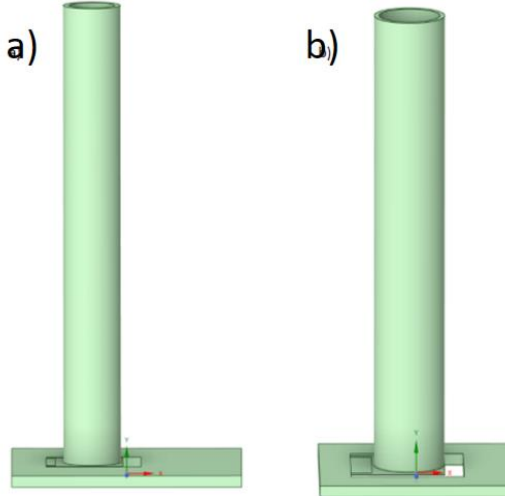


Figure 35 - a) 10mm Diameter PEH CAD Model b) 15mm Diameter PEH CAD Model

4.2.2 Bluff Body Vortex Frequency and Evaluation of Candidate Designs Frequencies

As described in the methodology of Section 3.2.2, both hand calculations and CFD simulations were completed to estimate the frequency of VIV under the near-shore underwater conditions of flow velocities ranging from $0.1 \text{ m/s} - 0.5 \text{ m/s}$. The symmetrical cross-section of the cylindrical bluff body means the same frequency of VIV is induced, no matter the direction of the fluid flow. These initial hand calculations are featured in Appendix C, which found a range of vortex frequencies between $2.2 \text{ Hz} - 11 \text{ Hz}$ and $1.47 \text{ Hz} - 7.33 \text{ Hz}$ for 10 mm and 15 mm circular cross sections, respectively. The more advanced CFD simulations completed to confirm these results are featured in Appendix D , which conclude similar results to those of the hand calculations, finding a VIV frequency range of $2.24 \text{ Hz} - 12.7 \text{ Hz}$ and $1.66 \text{ Hz} - 9.32 \text{ Hz}$ for the 10 mm and 15 mm diameter circles, respectively.

Optimal materials for the cantilever, piezoelectric material, and bluff body needed to be determined. The main factor considered when testing in these initial stages was the resultant natural frequency of the device, that is, how closely the natural bending frequencies match the VIV frequency the system would naturally undergo. Due to its widespread use and high effectiveness, a variant of Lead Zirconate Titanate (PZT), specifically both 5A and 5H were evaluated as the piezoelectric material instead of AlN, given their significantly higher power output. Due to their material properties, both beryllium copper and phosphor bronze were chosen to be tested to act as the cantilever beam. Finally, for simplicity, the material choice of the bluff body was selected as polystyrene, as it was known to work in the previous study of [29]. The ANSYS modal analysis completed for these materials is available in Table

2. These results strongly suggest that the natural frequency is heavily reliant on the dimensions of the system rather than the selected materials.

Table 2 - Natural Frequencies Depending on Materials

Test Number	Bluff body diameter (mm)	Cantilever material	Piezoelectric material	Natural bending frequency (Hz)	Natural torsional frequency (Hz)
1	10	Beryllium copper	PZT-5A	5.252	12.288
2	10	Beryllium copper	PZT-5H	5.261	12.325
3	10	Phosphor bronze	PZT-5A	5.051	11.900
4	10	Phosphor bronze	PZT-5H	5.060	11.938
5	15	Beryllium copper	PZT-5A	7.549	16.107
6	15	Beryllium copper	PZT-5H	7.576	16.174
7	15	Phosphor bronze	PZT-5A	7.303	15.599
8	15	Phosphor bronze	PZT-5H	7.329	15.666

These results determine that for the 10 mm and 15 mm bluff body diameters, material combinations 3 and 7, respectively, will act in harvesting power optimally. For this reason, only test numbers 3 and 7 will be used in the power output simulation analysis of Section 4.2.3.

4.2.3 Comparative Power Output of Candidate Designs

As per the methodology discussed in Section 3.2.3, two-way coupled simulations were conducted on the PEH designs determined by the results of Section 4.2.2 for water flow rates of 0.1, 0.3, and 0.5 m/s. The power output results for both PEHs under these conditions, with them applying the same 10^7 Ohm resistor as used in [29] are shown in Table 3. Furthermore, the simulations were run over a two-second duration, ensuring that the PEH stabilises and begins oscillating under natural conditions.

Table 3 - Power Output for 10mm and 15mm Bluff Body Diameter PEHs

Flow rate (m/s)	Single 10mm Power Output (W)	Single 15mm Power Output (W)
0.1	4.6001E-8	1.76983E-8
0.3	4.8972E-6	8.72605E-5
0.5	1.1017E-4	7.38363E-5

Furthermore, a graph of the power output of each PEH system compared to the previous system used in [29] is demonstrated in Figure 36.

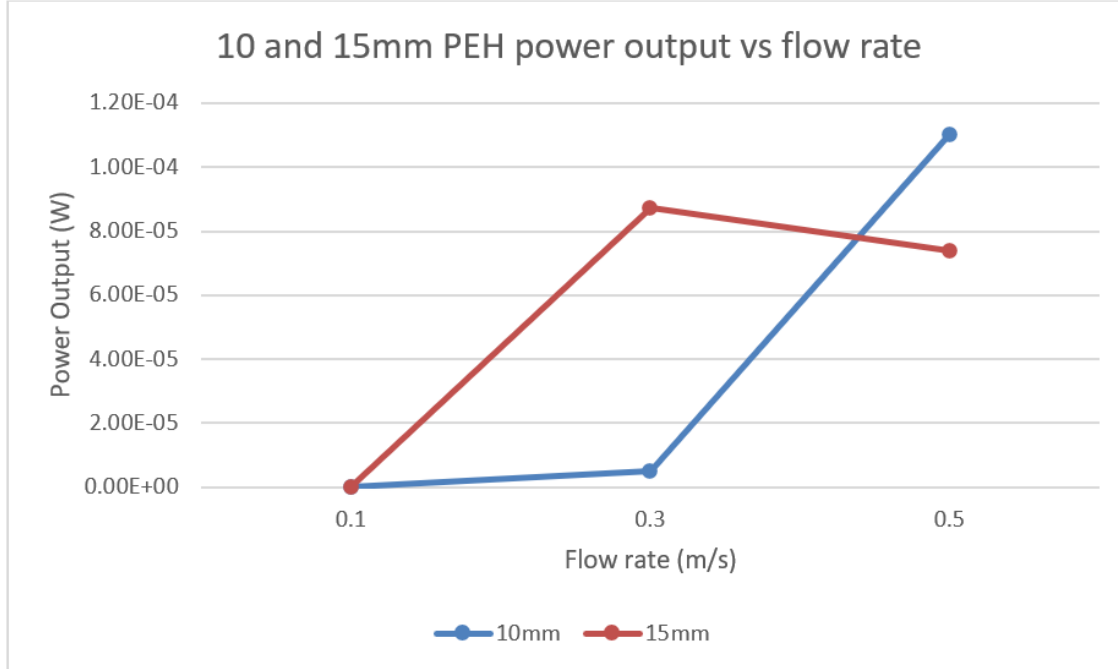


Figure 36 - 10 and 15mm PEH Power Output vs Flow Rate

The power output results conclude that the *10 mm* PEH achieves a higher power output at both *0.1 m/s* and *0.5 m/s* flow rates, while the *15 mm* PEH generates a greater power output for the flow rate of *0.3 m/s*. Since the PEH system is designed to optimise power output at lower flow rates, the results suggest that the *10 mm* PEH is a more suitable choice for integration into the multi-PEH configuration. This is due to the *10 mm* PEH design producing a 160% increase in power harvested compared to the *15 mm* design.

Furthermore, the velocity flow contours were also examined for the existence and strength of vortices shown in Figure 37. Higher-quality individual images of these contours are also available in Appendix E.

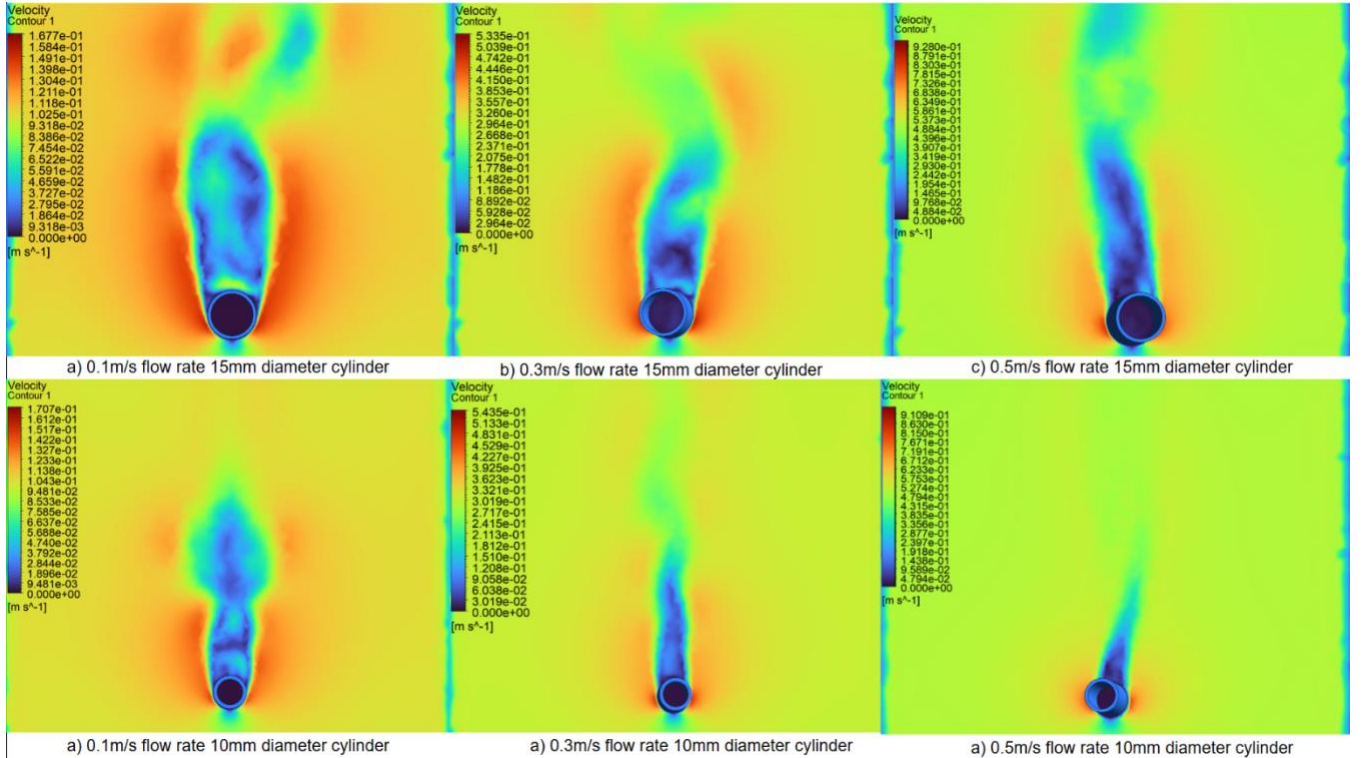


Figure 37 - Velocity Contours for Tested single PEH Configurations

These results demonstrate that no matter the bluff body cross-section or flow rate, each PEH generated vortices in its wake. However, the wakes provided by the *15 mm* design appear more volatile compared to the *10 mm* design, which could be beneficial in a multi-PEH system. This means that both designs would be suitable in enhancing the power output of subsequent PEHs in a multi-PEH system, but the *15 mm* design may act more optimally.

Due to the power output and vortices generated by the *10 mm* PEH design, it will be selected over the *15 mm* PEH design for use in the multi-PEH design of Milestone three.

4.3 M3 - Design and Simulation of Multi-PEH

4.3.1 Effect of Spacing on PEH Power Output

Due to the difference in PEH designs, the results of different sources conclude different distances as producing the most ideal power output. The previous PEH MEMs device [29] concluded that a ratio of $L/D \geq 4$ optimised the power. In contrast, [33] concludes that a spacing of $2D$ performs best and a spacing of $6D$ does not perform well for a parallel cantilever PEH system being used in a water-based environment involving two consecutive PEHs.

Furthermore, the meanings of the Length (L) and diameter (D) of the PEHs are demonstrated in Figure 38, with the purple circles denoting the bluff bodies themselves. Importantly, this diagram highlights that L is defined as the distance from the outmost edge of each bluff body rather than the distance between the centres of each bluff body.

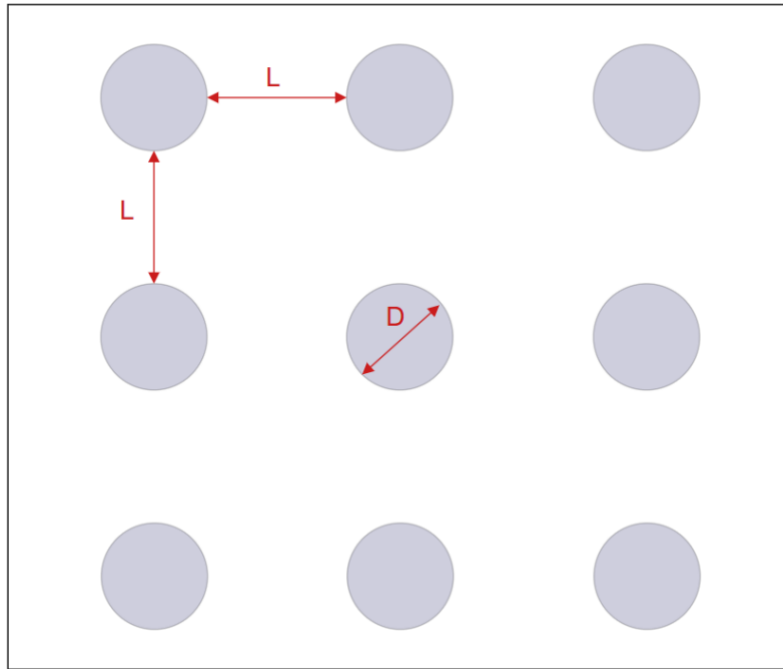


Figure 38 - Diagram Demonstrating L and D in Relation to PEH Bluff Bodies for a Three-by-Three Configuration

These varying results imply that power output simulations should be completed to determine the most optimal spacing, with spacing distances of $2D$, $3D$, and $4D$ being tested.

4.3.2 Simulated Power Output for Multiple PEH Configurations

The testing of the different configurations proved the effectiveness of sequentially aligning PEH systems to increase the power output of each individual PEH device. These results are highlighted in Table 4 and Figure 39, with each simulation being run over a two-second duration, providing sufficient time to ensure the system stabilises and begins to exhibit natural oscillatory behaviour.

Table 4 - Multi-PEH Power Output

Flow rate (m/s)	Single 10mm Power Output (W)	3by3 10mm 2D (W)	3by3 10mm 3D (W)	3by3 10mm 4D (W)
0.1	4.6001E-8	7.0402E-06	2.4789E-06	8.3596E-08
0.3	4.8972E-6	2.2629E-05	2.5094E-04	5.8837E-05
0.5	1.1017E-4	7.1501E-05	3.7390E-05	6.7895E-05

Table 4 demonstrates the variation in power output for different energy harvesting spacings, with the $2D$ spacing being most effective for a 0.1 m/s flow rate, $3D$ being most effective for a 0.3 m/s flow rate, and $2D$ again being the most effective for harvesting energy at a flow rate of 0.5 m/s , although as shown in Figure 39, the single PEH system harvests energy best for the 0.5 m/s flow rate, even when compared to all sequential type energy harvesting systems.

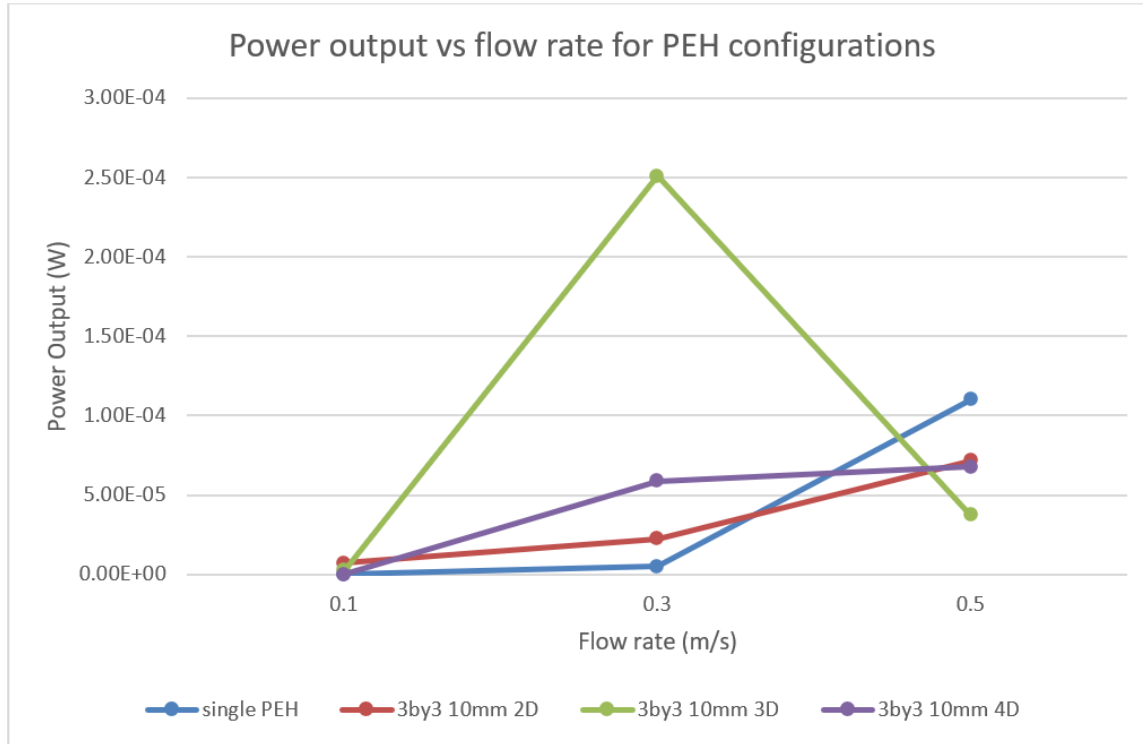


Figure 39 - Power Output vs Flow Rate for PEH Configurations

Again, since harvesting energy in lower flow rate environments is the target of the designed PEH system, the $2D$ spacing is the most suitable for this application, given its performance compared to the other spacings at a flow rate of 0.1 m/s . The $2D$ spacing can be calculated as performing 184% and 8323% better than the $3D$ and $4D$ spacings, respectively, at the 0.1 m/s flow rate. Even though the $3D$ spacing for this design performs significantly better than all other spacings for a flow rate of 0.3 m/s , as demonstrated in Figure 39, the limited performance in the other two simulated flow rates means that it will not be implemented in the final design.

Although a spacing of $4D$ did not do well in harvesting power optimally, the results concluded from the velocity contours of the given spacing were of some importance. This is shown in Figure 40, where the trail of vortices produced from each bluff body at the point at which they are impacting the next sequential bluff body is minimal for the $4D$ spaced simulations (Figure 40 – g, h, i).

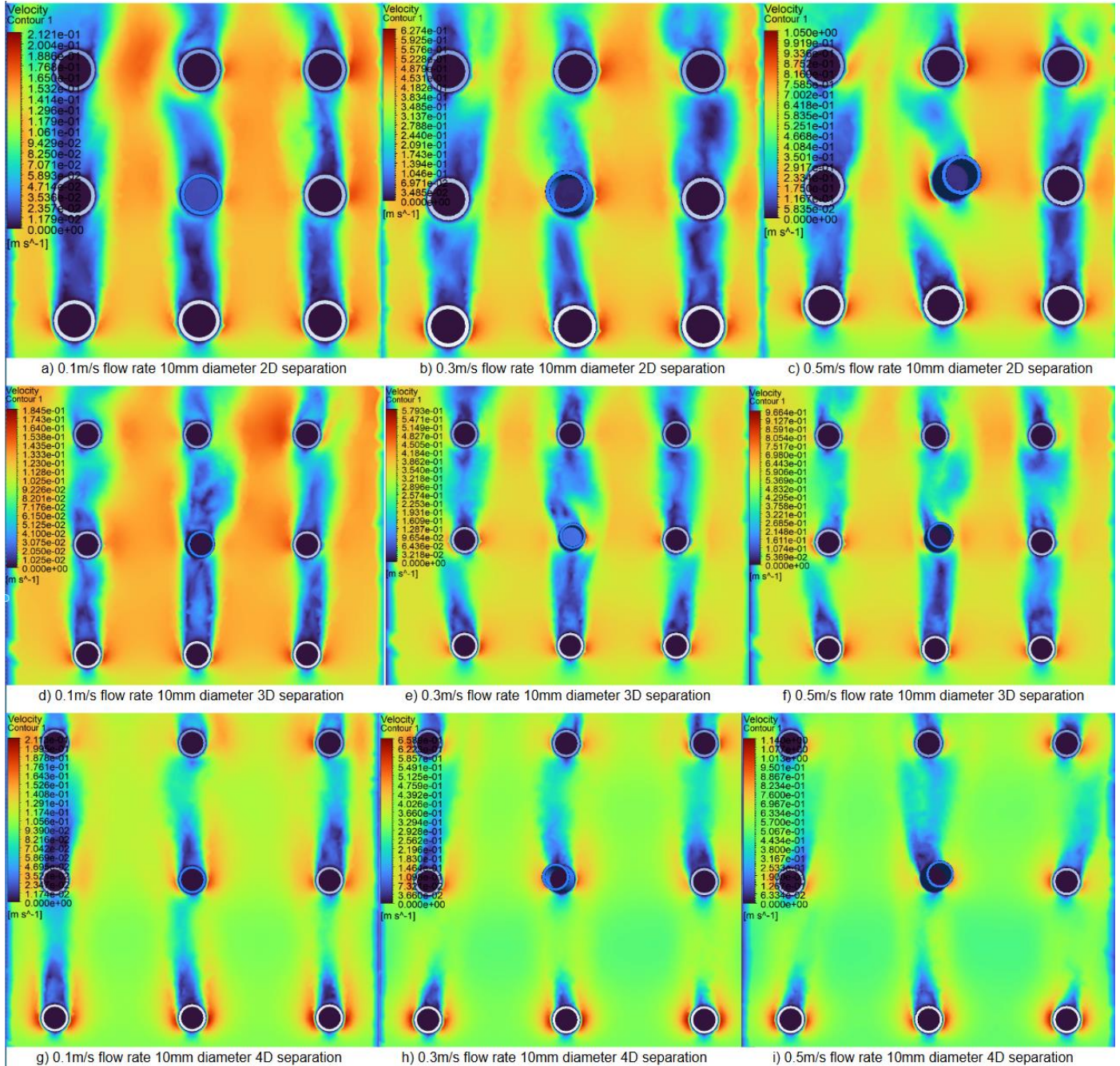


Figure 40 - Velocity Contours for Evaluated Multi-PEH Configurations

Higher-quality images of these velocity contours are available in Appendix F.

This 4D spacing would enable the flow after each bluff body to almost reset to what it was when it initially entered the energy harvesting system, allowing the system to reuse a spacing of 2D to harvest flow rates of 0.1 m/s more efficiently. This arrangement of PEH spacings is demonstrated in Figure 41 and will be implemented in the overall layout of the multi-PEH design.

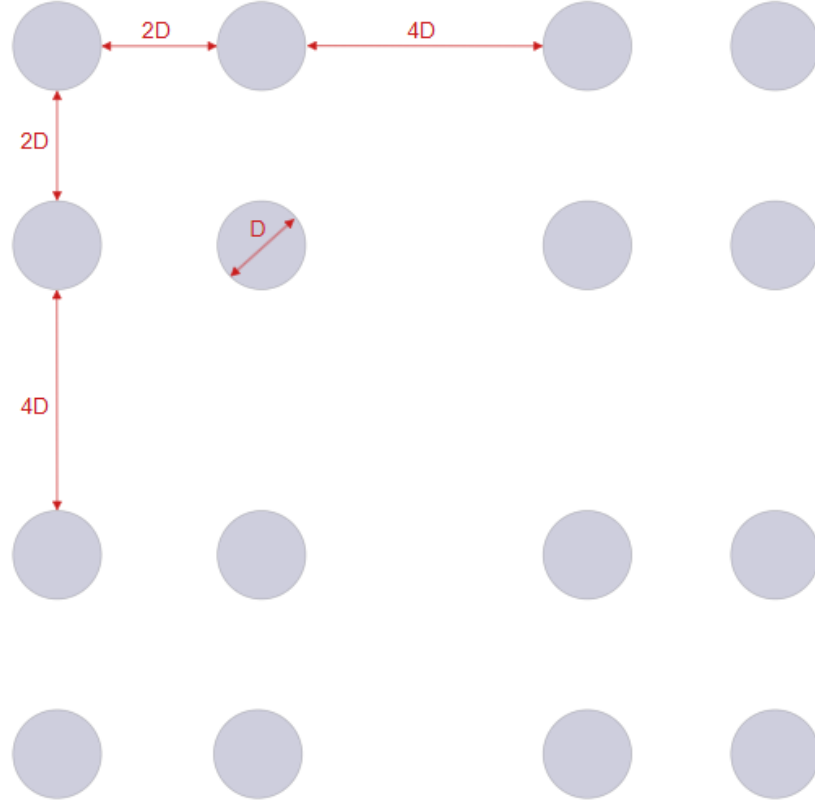


Figure 41 - Small-scale Arrangement of how PEHs will be Arranged

Furthermore, by expanding this arrangement to cover the entirety of the PEHs area, the following design presented in Figure 42 can be established. This design contains a total of 60 individual PEHs. When the current is flowing in either the forward or backward direction, 10 will act as single PEHs, 30 will give a power output resulting from a 2D spacing, and 20 will act with a spacing of 4D. For a sideways current flow, 6 will act as single PEHs, 30 will act as 2D spaced PEHs, and 24 will act as 4D spaced PEHs.

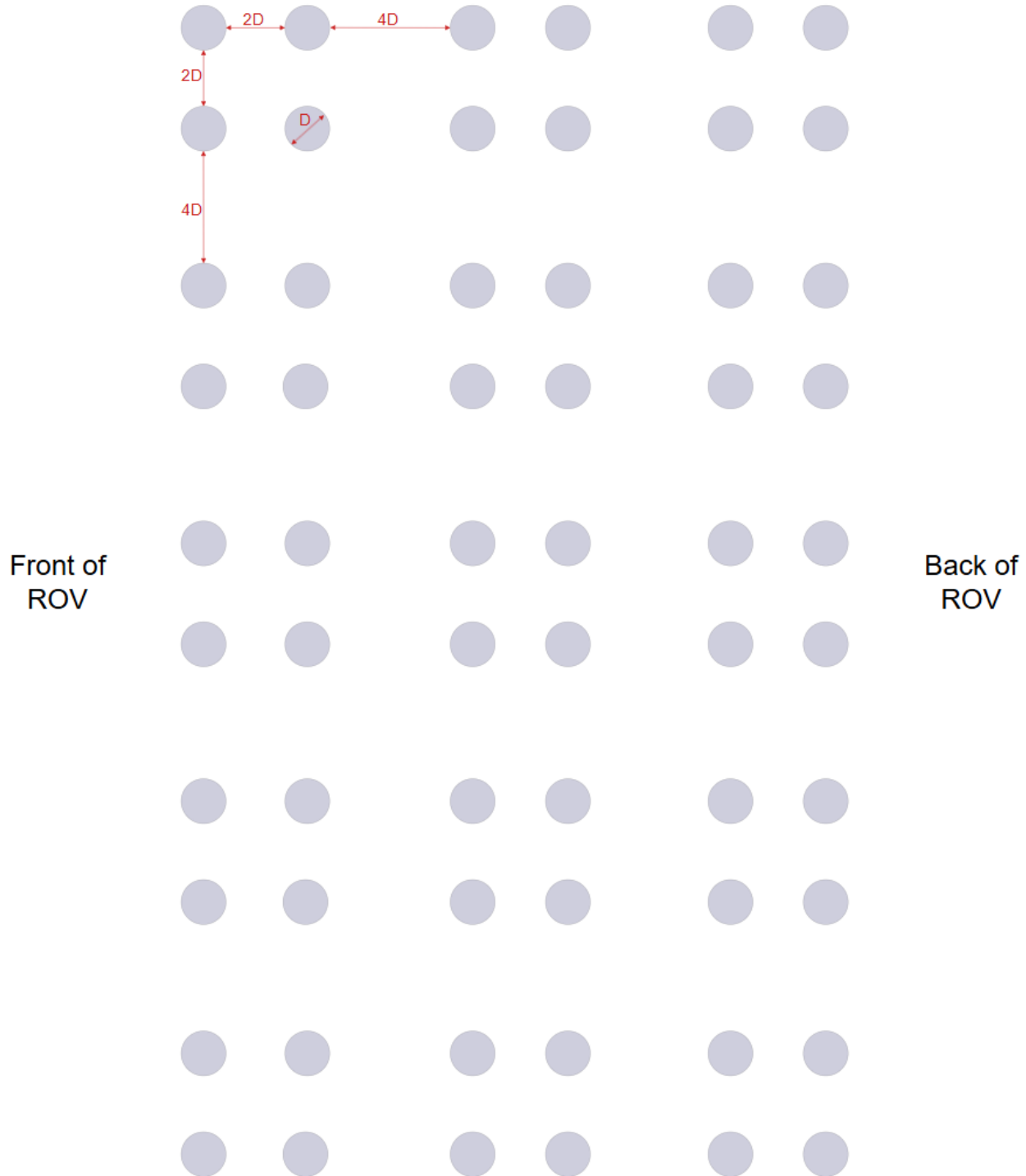


Figure 42 - Entire Multi-PEH Layout for Overall ROV

Through this spacing, the final power output of the given design configuration can be estimated for any given flow rate. These final power outputs are calculated in Table 5, and

Table 6 where it is concluded that the current flowing sideways harvests energy more efficiently.

Table 5 - Power Output for Forward and Backward Current Flow

Flow rate (m/s)	Power output from SPEHs (W)	Power output from 2D spacing (W)	Power output from 4D spacing (W)	Total Power output (W)
0.1	4.6001E-7	2.1121E-4	1.6719E-6	2.3253E-4
0.3	4.8972E-5	6.7888E-4	1.1767E-3	1.9046E-3
0.5	6.6102E-4	2.1450E-3	1.3579E-3	4.1639E-3

Table 6 - Power Output for Sideways Current Flow

Flow rate (m/s)	Power output from SPEHs (W)	Power output from 2D spacing (W)	Power output from 4D spacing (W)	Total Power output (W)
0.1	2.7601E-7	2.1121E-4	2.0063E-6	2.1349E-4
0.3	2.9383E-5	6.7888E-4	1.4121E-3	2.1201E-3
0.5	6.6102E-4	2.1450E-3	1.6295E-3	4.4355E-3

Figure 43 also highlights this by demonstrating that the sideways flow power harvested is slightly above that of the forward flow for the three simulated flow rates.

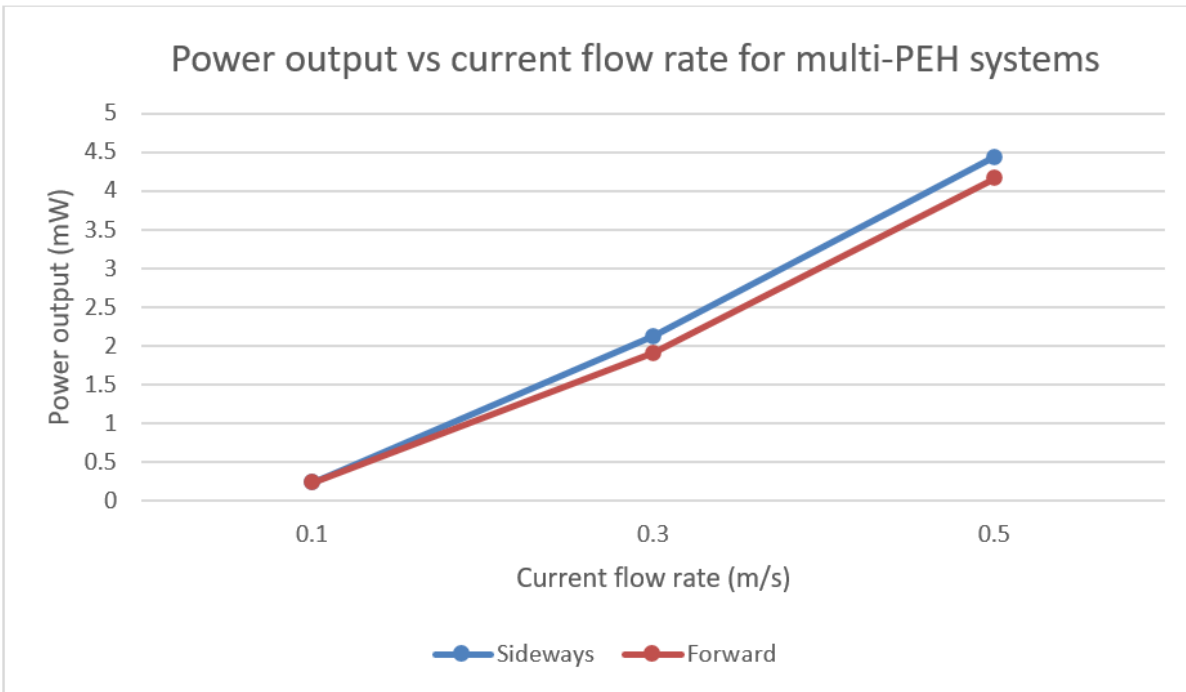


Figure 43 - Graph for Power Output vs Current Flow Rate for Multi-PEH Systems

These results indicate that only a 0.5 m/s sideways current flow would be able to continuously power the ROV's beacon, which had an estimated power consumption of 4.17 mW . However, forward or backward flows at the same speed produce outputs that fall within an acceptable range of this estimate, suggesting they could also sustain the beacon's operation. Other flow rates in different current directions would require intermittent powering of the beacon through the use of a battery or super capacitor.

4.4 M4 - Design and Testing of Multi-PEH Container/Shell

4.4.1 Shell Design Decisions Regarding Dimensions and Sizing

From the multi-PEH final design layout discussed in Section 4.3.2 and shown in Figure 42, the width and length of the total PEH spacing can be determined as 360 mm and 200 mm , respectively. Since the width between the fixture points is 340 mm , the PEHs can be fitted easily between these fixture points. Furthermore, as discussed in Section 3.4.1, the maximum length of the device is limited to 457.1 mm , which means that the current PEH assembly length of 360 mm is well within this limit. The final limitation to dimensions is discussed briefly in Section 3.1.1. The final height of the design, ignoring fixture points, should be limited to 100 mm , which will be considered in the design choices made in Section 4.4.2.

4.4.2 Shell Material and Shape Selection

The final shell design without the PEHs attached is demonstrated in Figure 44, with the shape of the shell designed in a way that would limit the effects of drag on the motion of the BlueROV2, to which it will be attached. Essential features in the design include curved surfaces to minimise the drag coefficient and drag force, as well as the design being symmetric in the forward and sideways directions, such that when moving forwards and backwards or left and right, the ROV would perform consistently the same. Aerofoil and hydrofoil-type shapes were excluded from the design due to their asymmetrical nature, which would result in inconsistent drag forces depending on the ROV's direction of travel. Further drag analysis to determine the performance of such a design is completed in Section 4.4.3 of this report.

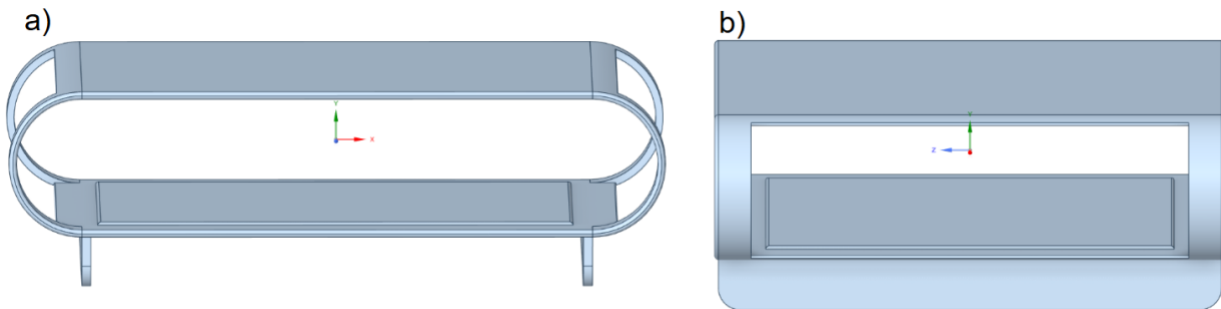


Figure 44 - a) PEH Shell Front View b) PEH Shell Side View

Suitable materials for the given situation were then evaluated. These materials included polycarbonate (PC), Polylactic Acid (PLA), Aluminium 6061, and Acrylonitrile Butadiene Styrene (ABS). These materials were evaluated regarding their density, water absorption, mechanical strength, Corrosion Resistance, Ease of Fabrication, and cost shown in Table 7.

Table 7 – Comparison of Material Properties

Material Property	PC	ABS	PLA	Aluminium 6061
Water Absorption	Low	Moderate	High	None
Density (g/cm³)	1.2	1.04	1.25	2.70
Mechanical strength	High	Moderate	Low	Very High
Corrosion resistance	High	Moderate	Very Low	Moderate
Ease of Fabrication	High	High	High	Moderate
Cost	Moderate	Low	Very Low	High

Table 7 highlights that ABS and PLA are not very suitable for the specified application due to their poor mechanical strength and corrosion resistance compared to the other two materials. Furthermore, even though Aluminium 6061 does not absorb any water, its greater density could affect the motion of the ROV due to a significantly greater weight compared to any of the other materials evaluated. For this reason, PC will be chosen as the material for the shell of the PEH system.

Using CAD software, the overall volume of the shell was determined to be 1705404.68 mm^3 . From this, the maximum mass of the shell using PC can be calculated as follows:

$$\text{Mass}_{\text{shell}} = 1.2 \times \frac{1705404.68}{1000} = 2046,48 \text{ g} \approx 2.05 \text{ kg}$$

The BlueROV2 heavy edition weighs approximately 11.5 kg . Therefore, the total weight of the PEH shell will be at a maximum of 18% of the ROV's mass. This mass percentage increase would be successful in limiting the effects of the PEH system on the motion of the ROV, as the BlueROV2 heavy is capable of carrying masses up to 6.8 kg [43].

4.4.3 Results of Drag Simulation Testing

After conducting the drag force simulations mentioned in Section 3.4.3, the following data in Table 8 can be derived. This table demonstrates the percentage of drag force generated by the PEH system shown in Figure 45, compared to the total calculated drag force induced by the ROV.

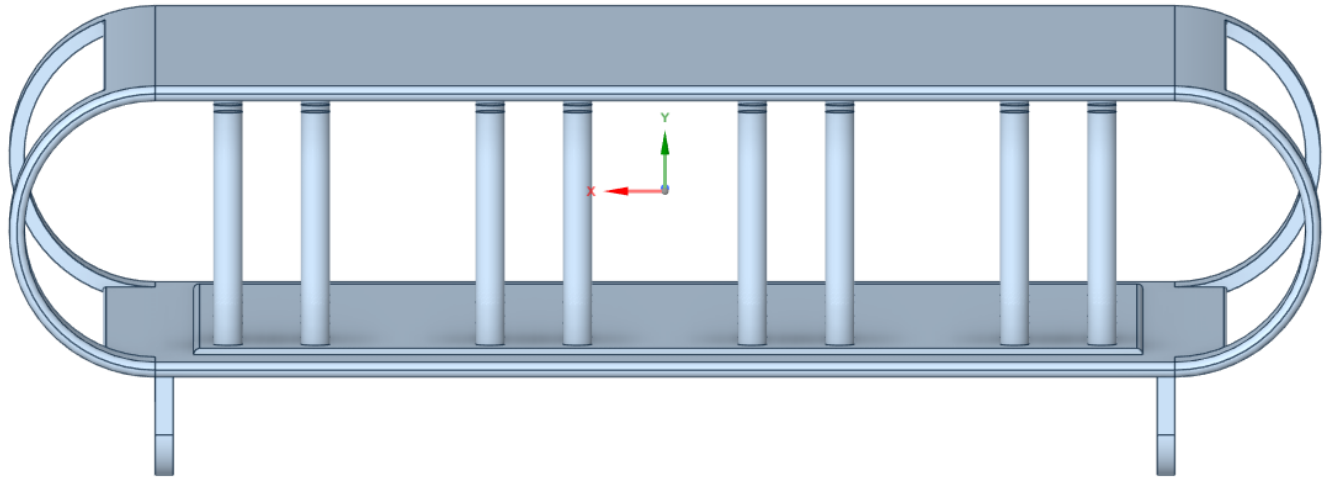


Figure 45 - CAD Model used for Drag Testing

Table 8 - Simulated Drag for Shell and Calculated Drag for ROV at Varying Flow Rates

Flow rate (m/s)	Calculated Drag force for ROV (N)	Simulated Drag force for PEH (N)	Percentage
0.25	12.2375	0.54002	4.41%
0.50	42.1	2.0915	4.97%
0.75	89.5875	4.6137	5.15%
1.00	154.7	8.0570	5.21%
1.25	237.4375	12.556	5.29%
1.50	337.8	17.969	5.32%

Section 3.4.3 establishes that the drag induced by the shell should be less than 10% of the drag induced by the whole ROV. This is true for all simulated flow rates, with the average percentage over all flow rates being 5.06%. Therefore, the shell design is successful in minimising the effects of the PEH system on the ROV's movement.

Furthermore, the paths of fluid flow were evaluated for the simulated design to determine if any vortices were forming outside of those from the bluff body, which could impede the motion or control of the ROV. No vortices were found in any of the simulated tests, with an example fluid path demonstrated in Figure 46. This outcome further emphasises the successful implementation of the designed solution.

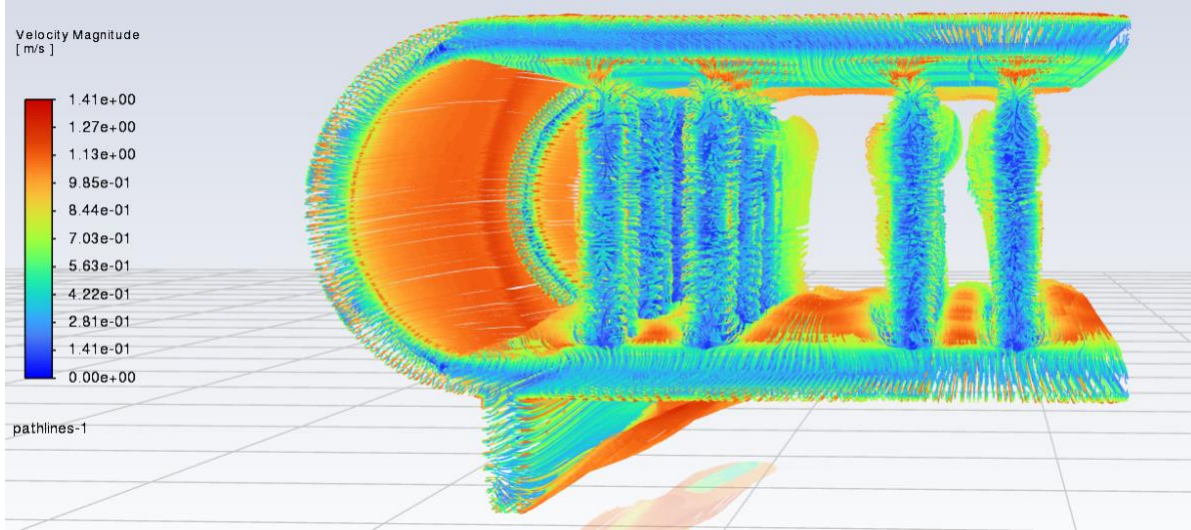


Figure 46 – Example Fluid Path Lines for Drag Simulations

4.5 Discussion

Milestone one results successfully validate the previous report [29], although this validation was limited by the number of testing wind flow velocities that were used. That is, only a singular wind flow velocity was tested to attempt to recreate the maximum power output, and future testing should be completed at varying flow rates mirroring that of Figure 33, to further increase the reliability and accuracy of simulated results. Furthermore, Milestone two results were limited by the lack of test cases and model configurations. Although the natural frequencies of the PEH models selected for two-way coupled testing were close to those of VIV, adjustments to the model could be made to better align them. Future modelling for this should also involve testing each model's power output instead of only selecting a handful that had natural frequencies aligning closest to the VIV frequency of each structure. Multi-PEH testing completed in Milestone three was limited by ANSYS student technology, as two-way coupled simulations only allowed for a limited number of mesh elements, meaning only a singular central PEH could be made to be dynamic. This meant that the results of Milestone three may not be exactly representative of what would occur in physical experimental testing. In the future, different CFD and mechanical simulation software should be used so that the simulations better represent the real world. Finally, Milestone four was limited by the number of flow directions. That is, only a flow passing directly through the model from the front side was tested. In future, further tests should take place that place the direction of water flow at varying angles passing through the PEH shell.

Next steps for this work would primarily involve completing more detailed simulations with more flow rates, such that an ideal PEH type and multi-PEH configuration can be selected. Using this design, physical experimental tests should be conducted to validate simulated results and further prove the effectiveness of such a design.

5 Conclusions

The thesis can be seen as successful in designing a low-power underwater PEH system that uses VIV to power the given beacon. The results of simulations and testing allowed for conclusions to be made in each of the four milestones of this report.

The results of simulations in Milestone one successfully validated and proved the success of the two-way coupled simulation methods, with the concluded power output being within a reasonable range of the experimental results. That is, the simulation's power output results were within 50% of the initial experimental results. Furthermore, these simulations also acted in concluding the low effectiveness of the previous design due to the significant disparity between the natural frequency and the VIV frequency of the given PEH.

Additionally, Milestone two's results determined the most suitable design for a singular PEH, concluding that the 10 mm diameter cylindrical bluff body utilising phosphor bronze as the cantilever and PZT-5A as the piezoelectric material had a natural frequency which aligned closest to the VIV generated by the given bluff body. Furthermore, the results of simulations in this milestone also concluded that the previously mentioned combination was the most suitable regarding power output at low flow rates, establishing it as the singular PEH design that would make up the multi-PEH system.

Milestone three results further emphasised the effectiveness of the singular PEH design, with it determining the overall best combination/layout of PEHs, which would harvest energy most effectively for the given criteria. These results concluded that a combination of 2D and 4D spacing was most suitable and proved that the system met the power requirements of the designated beacon, which would also be attached to the ROV. It was concluded that, under steady sideways flow conditions of 0.5 m/s, the final system is capable of continuously powering the 4.17 mW emergency beacon, with the harvested power exceeding consumption by approximately 0.27 mW. Alternatively, in lower sideways flow scenarios where power output may drop, the system would require approximately two hours or 19.6 hours of continuous charging at flow rates of 0.3 m/s or 0.1 m/s, respectively, to provide one hour of beacon operation. Under forward and backwards flow conditions, the system produced a peak power output of 4.16 mW at 0.5 m/s, effectively meeting the beacon's power requirements, making it capable of continuous beacon operation. At lower forward and backward flow rates of 0.3 m/s and 0.1 m/s, the output decreased to 1.90 mW and 0.233 mW, requiring approximately 2.8 and 17.9 hours of charging, respectively, to achieve one hour of beacon operation.

Finally, Milestone four results fulfilled the goal of designing a shell for the system that would have minimal impacts on the motion of the ROV. Polycarbonate was selected as the optimal material for the given use case due to its

relatively light weight and water resistance. Furthermore, the results of drag force simulations indicated that PEH system induced an average drag force of 5.06% of the ROV's total drag, making it highly suitable for the given use case.

These conclusions demonstrate the overall success of the project in meeting all initial objectives. Specifically, the project successfully designs an effective low-power underwater PEH system that harnesses energy from induced VIV while minimising interference with the movement of the ROV to which it is attached.

6 References

1. International, R. *ULB-362PL Underwater Beacon With Power Loss*. 23/10/2024]; underwater beacon with power loss activation]. Available from: <https://www.rjeint.com/portfolio/ulb-362pl-underwater-beacon-power-loss/>.
2. International, R. *ULB-364 General Purpose Acoustic Beacon*. ULB-364 General Purpose Acoustic Beacon for underwater ROVs]. Available from: <https://www.rjeint.com/portfolio/ulb-364-general-purpose-acoustic-beacon/>.
3. Renner, B.-C., J. Heitmann, and F. Steinmetz, *AHOI: Inexpensive, low-power communication and localization for underwater sensor networks and μAUVs*. ACM Transactions on Sensor Networks (TOSN), 2020. **16**(2): p. 1-46.
4. Ortiz, A., et al. *Improving the safety of AUVs*. in *Oceans' 99. MTS/IEEE. Riding the Crest into the 21st Century. Conference and Exhibition. Conference Proceedings (IEEE Cat. No. 99CH37008)*. 1999. IEEE.
5. Adu-Manu, K., et al., *Energy-harvesting wireless sensor networks (EH-WSNs): A review*. ACM Transactions on Sensor Networks, 2018. **14**: p. 1-50.
6. Vignesh, S., et al. *Analysis on energy harvesting techniques for underwater wireless sensor networks*. in *2021 Third international conference on intelligent communication technologies and virtual mobile networks (ICICV)*. 2021. IEEE.
7. Surmenev, R.A., et al., *Hybrid lead-free polymer-based nanocomposites with improved piezoelectric response for biomedical energy-harvesting applications: A review*. Nano Energy, 2019. **62**: p. 475-506.
8. Trento, C. *A Closer look at Piezoelectric Crystal*. Available from: [https://www.samaterials.com/content/a-closer-look-at-stressed-piezo-crystals.html#:~:text=Crystal%20Structure%20Characteristics%20of%20Piezoelectric%20Crystals&text=The%20electric%20dipoles%20\(consisting%20of,do%20not%20exhibit%20macroscopic%20polarization](https://www.samaterials.com/content/a-closer-look-at-stressed-piezo-crystals.html#:~:text=Crystal%20Structure%20Characteristics%20of%20Piezoelectric%20Crystals&text=The%20electric%20dipoles%20(consisting%20of,do%20not%20exhibit%20macroscopic%20polarization).
9. Design, E. *What is the piezoelectric effect?* ; Available from: <https://www.electronicdesign.com/technologies/power/article/21801833/what-is-the-piezoelectric-effect>.
10. Wang, H., et al. *Mechanical strength responses of poled lead zirconate titanate under extreme electric field and various temperature conditions*. in *ASME International Mechanical Engineering Congress and Exposition*. 2016. American Society of Mechanical Engineers.
11. Shin, Y.-H., et al., *Mechanical fatigue resistance of piezoelectric PVDF polymers*. Micromachines, 2018. **9**(10): p. 503.
12. Guo, X., et al., *Piezoelectric Properties of 0-3 Composite Films Based on Novel Molecular Piezoelectric Material (ATHP) 2PbBr4*. Materials, 2022. **15**(18): p. 6378.
13. Xuepeng Fu, S.F., Zhaolong Han, Zhibo Niu, Mengmeng Zhang, Bing Zhao,, *Numerical simulations of 2-DOF vortex-induced vibration of a circular cylinder in two and three dimensions: A comparison study*. Journal of Ocean Engineering and Science, 2023.
14. Raghavan, K. and M. Bernitsas, *Experimental investigation of Reynolds number effect on vortex induced vibration of rigid circular cylinder on elastic supports*. Ocean Engineering, 2011. **38**(5-6): p. 719-731.
15. Gu, J., A.C. Fernandes, and J.S. Sales Jr, *Alternative insight to understand the Reynolds number effects in vortex-induced vibration*. Marine Structures, 2020. **69**: p. 102686.
16. Wang, X., et al., *Experimental investigation of flow past a confined bluff body: Effects of body shape, blockage ratio and Reynolds number*. Ocean Engineering, 2021. **220**: p. 108412.
17. Gu, M., et al., *The effects of submergence depth on Vortex-Induced Vibration (VIV) and energy harvesting of a circular cylinder*. Renewable Energy, 2020. **151**: p. 931-945.
18. Molino-Minero-Re, E., et al. *Piezoelectric energy harvesting from induced vortex in water flow*. in *2012 IEEE International Instrumentation and Measurement Technology Conference Proceedings*. 2012. IEEE.
19. Sui, G., et al., *An underwater piezoelectric energy harvester based on magnetic coupling adaptable to low-speed water flow*. Mechanical Systems and Signal Processing, 2023. **184**: p. 109729.
20. Shah, M.M., et al., *Investigation of Bluff Body Size Effects on Piezoelectric Performance Using Flow-Induced Vibration*. Engineering Proceedings, 2024. **75**(1): p. 21.
21. Aramendia, I., et al., *Oscillating U-shaped body for underwater piezoelectric energy harvester power optimization*. Micromachines, 2019. **10**(11): p. 737.
22. Kim, S., et al., *Propeller-based underwater piezoelectric energy harvesting system for an autonomous IoT sensor system*. Journal of the Korean Physical Society, 2020. **76**: p. 251-256.
23. Zhao, L.-C., et al., *A water-proof magnetically coupled piezoelectric-electromagnetic hybrid wind energy harvester*. Applied Energy, 2019. **239**: p. 735-746.
24. Su, W.-J. and W.-Y. Lin, *Design and analysis of a vortex-induced bi-directional piezoelectric energy harvester*. International Journal of Mechanical Sciences, 2020. **173**: p. 105457.
25. Su, W.-J. and Z.-S. Wang, *Development of a non-linear bi-directional vortex-induced piezoelectric energy harvester with magnetic interaction*. Sensors, 2021. **21**(7): p. 2299.
26. Karim, M.A. and Z.I. Awal, *An Ocean Wave Energy Harnessing Model Using Piezo-Electric Device*.
27. Toma, D.M., et al. *An impacting energy harvester through piezoelectric device for oscillating water flow*. in *MARTECH 2013: 5th International Workshop on Marine Technology: 19th-20th of November, Vilanova i la Geltrú*. 2013.
28. Toma, D., et al. *An impacting energy harvester through piezoelectric device for velocity water flow*. in *Martech 2013 5th International Workshop on Marine Technology*. 2013. SARTI.
29. Lee, Y.J., Qi, Y., Zhou, G. et al., *Vortex-induced vibration wind energy harvesting by piezoelectric MEMS device in formation*. Sci Rep 9, 2019.

B. McMillen – Low Power Energy Harvesting System for Underwater Beacons on ROVs

30. Wang, J., et al., *A cross-coupled dual-beam for multi-directional energy harvesting from vortex induced vibrations*. Smart Materials and Structures, 2019. **28**(12): p. 12LT02.
31. Hai, W., et al. *Research and design of broadband underwater flow induced vibration energy harvester based on Karman vortex*. in *2018 IEEE 13th Annual International Conference on Nano/Micro Engineered and Molecular Systems (NEMS)*. 2018. IEEE.
32. Hu, Y., et al., *Modeling and experimental study of a piezoelectric energy harvester from vortex shedding-induced vibration*. Energy conversion and management, 2018. **162**: p. 145-158.
33. Shan, X., et al., *Enhancing the performance of an underwater piezoelectric energy harvester based on flow-induced vibration*. Energy, 2019. **172**: p. 134-140.
34. Aramendia, I., et al., *Power control optimization of an underwater piezoelectric energy harvester*. Applied Sciences, 2018. **8**(3): p. 389.
35. Mehdipour, I., et al., *Comprehensive experimental study on bluff body shapes for vortex-induced vibration piezoelectric energy harvesting mechanisms*. Energy Conversion and Management: X, 2022. **13**: p. 100174.
36. Li, H., et al., *Dynamics and performance evaluation of a vortex-induced vibration energy harvester with hybrid bluff body*. Smart Materials and Structures, 2023. **32**(4): p. 045016.
37. Wang, J., et al., *Enhancing vortex-induced vibrations of a cylinder with rod attachments for hydrokinetic power generation*. Mechanical Systems and Signal Processing, 2020. **145**: p. 106912.
38. *Piezoelectric Constitutive Equations*. Available from: <https://onlinelibrary.wiley.com/doi/pdf/10.1002/9781119991151.app1>.
39. *Waves and nearshore currents*. Available from: <https://www.seagrant.wisc.edu/our-work/focus-areas/coastal-processes-and-engineering/coastal-processes/waves-and-nearshore-currents/>.
40. von Benzon, M., et al., *An Open-Source Benchmark Simulator: Control of a BlueROV2 Underwater Robot*. Journal of Marine Science and Engineering, 2022. **10**(12): p. 1898.
41. Fossen, T.I., *Handbook of Marine Craft Hydrodynamics and Motion Control*. 2011.
42. Fraga, M.A., et al., *Wide bandgap semiconductor thin films for piezoelectric and piezoresistive MEMS sensors applied at high temperatures: an overview*. Microsystem technologies, 2014. **20**(1): p. 9-21.
43. *Payload limit of Heavy*. 2018; Available from: <https://discuss.bluerobotics.com/t/payload-limit-of-heavy/2680>.
44. *Energizer 9V battery product Data sheet*. Energizer 9V battery product Data sheet]. Available from: <https://data.energizer.com/pdfs/max-eu-9v.pdf>.
45. Ellingsen, Ø.M., et al., *Twin Strouhal numbers in pressure loading of circular cylinder at high Reynolds numbers*. Journal of Fluids and Structures, 2022. **115**: p. 103782.
46. Manal, Y. and P. Hémon, *Unsteady loads on circular cylinder in cross-flow: an observation in natural wind and comparison with wind tunnel experiments*. Journal of Fluids and Structures, 2024. **124**: p. 104019.

7 Appendices

Appendix A

The ULB-364 implements two 9 V batteries with a volume of 21.1 cm^3 and capacity of 500 mAh [44]. Using this data, the Total Energy supplied by the batteries over the 90 days can be calculated as follows:

$$\text{Total Energy} = 9V \times (0.5 \times 2) = 9\text{Wh}$$

Furthermore, the total power consumption over this period (90 days = 2160 hours) can then be calculated:

$$\text{Power} = \frac{\text{Total Energy}}{\text{Time}} = \frac{9 \text{ Wh}}{2160 \text{ hours}} = 4.17 \text{ mW}$$

Hence, meaning that the beacon uses 4.17 mW continuously while in operation. Finally, the power density of the device can then be calculated as follows:

$$\text{Total Volume} = 2 \times 21.1 \text{ cm}^3 = 42.2 \times 10^{-6} \text{ m}^3$$

$$\text{Power Density} = \frac{4.17 \text{ mW}}{42.2 \times 10^{-6} \text{ m}^3} = 98.76 \text{ W/m}^3$$

Appendix B

As explained in the report, the dimensions for each PEH were based on the factor of the increase in the diameter of the bluff body's cross-section. This meant that the *10 mm* diameter dimensions increased by a factor of 5 and the *15 mm* diameter dimensions increased by a factor of 7.5.

Table 9- Single PEH Dimensions

	Original PEH from [29]	10mm diameter dimensions	15mm diameter dimensions
Cantilever length	<i>2.660 mm</i>	<i>13.3 mm</i>	<i>19.95 mm</i>
Cantilever width	<i>2.470 mm</i>	<i>12.35 mm</i>	<i>18.525 mm</i>
Cantilever height	<i>10 μm</i>	<i>50 μm</i>	<i>75 μm</i>
Piezo material length	<i>2.038 mm</i>	<i>10.19 mm</i>	<i>15.285 mm</i>
Piezo material width	<i>0.324 mm</i>	<i>1.62 mm</i>	<i>4.86 mm</i>
Piezo material height	<i>0.5 μm</i>	<i>0.03 mm</i>	<i>0.03 mm</i>
Bluff body diameter	<i>2 mm</i>	<i>10 mm</i>	<i>15 mm</i>
Bluff body height	<i>10 mm</i>	<i>80 mm</i>	<i>80 mm</i>

Appendix C

The formula for vortex shedding frequency is as follows: where St is the Strouhal number, u is the fluid velocity, and D diameter of the bluff body.

$$f_v = \frac{St \cdot u}{D}$$

Both [45] and [46] conclude that cylinder/circular-shaped bluff bodies have an approximate Strouhal number ranging between 0.2 and 0.24. The Reynolds number of a system affects the Strouhal number, but only for extremely high or low values. Since the Reynolds number of the system being considered only ranges from 1500 to 7500, it is assumed the Strouhal number will remain unchanged as these values are neither too high nor too low. Taking the average of this gives a Strouhal number of 0.22, and then substituting into the equation and evaluating for flow rates ranging from 0.1 m/s to 0.5 m/s gives the results presented in Table 10.

Table 10 - VIV Frequency for 0.1m/s to 0.5m/s Water Flow

Flow rate of water (m/s)	10mm diameter Vortex Shedding Frequency (Hz)	15mm diameter Vortex Shedding Frequency (Hz)
0.1	2.2	1.47
0.2	4.4	2.93
0.3	6.6	4.4
0.4	8.8	5.87
0.5	11	7.33

Appendix D

This Appendix implements methods discussed in Section 3.1.3 to determine the vortex shedding frequencies of each bluff body cross-section at various flow rates.

At 0.1 m/s for the 15 mm bluff body, the lift force acting on the cross-section is analysed and shown in Figure 47.

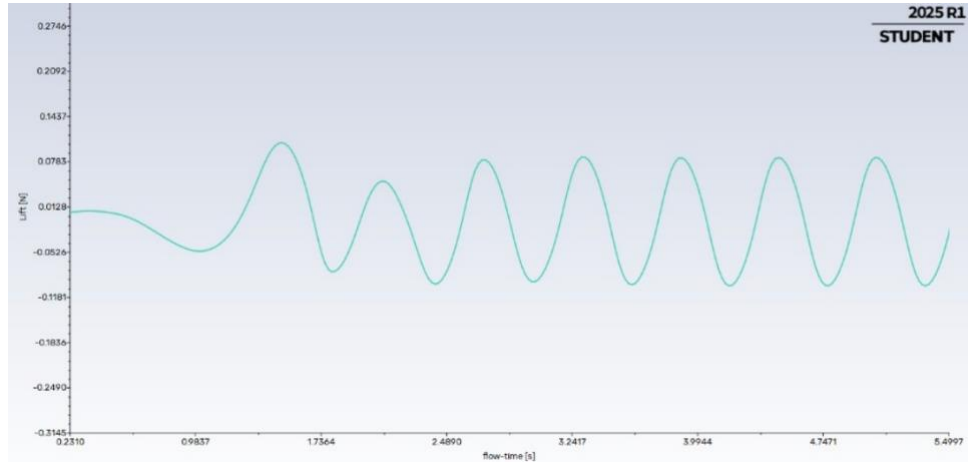


Figure 47 – VIV Lift Force at 0.1m/s , 15mm Diameter

This gives a result of 1.66 Hz as the vortex shedding frequency for a flow rate of 0.1 m/s when a Fourier analysis is completed Figure 48.

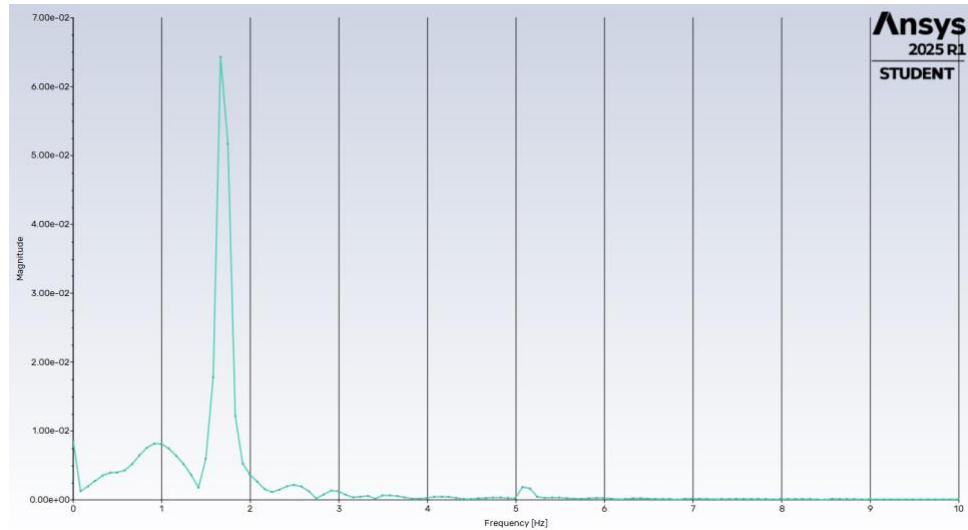


Figure 48 – ANSYS Fourier Analysis for VIV Frequency at 0.1m/s , 15mm Diameter

Repeating the same process for a 15 mm at 0.5 m/s system is demonstrated in Figure 49.

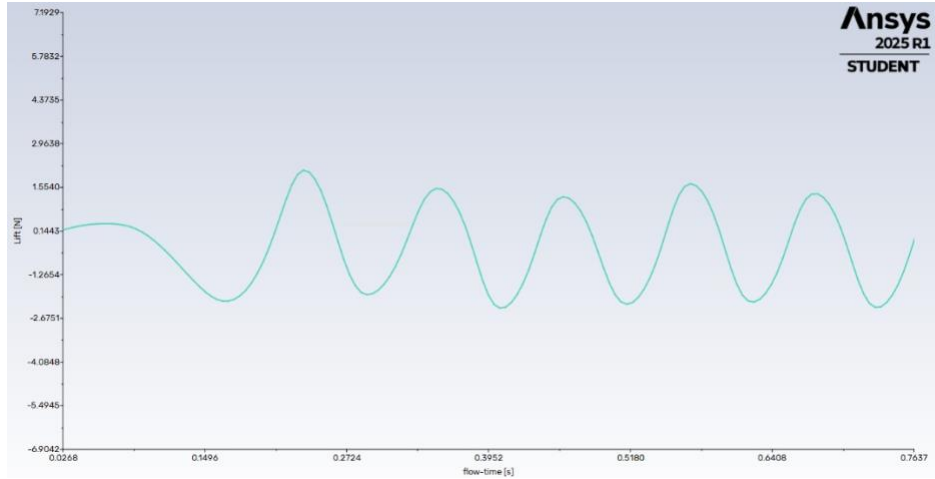


Figure 49 – VIV Lift Force at 0.5m/s, 15mm Diameter

This gives a result of 9.32 Hz as the vortex shedding frequency for a flow rate of 0.5 m/s when completing the Fourier analysis shown in Figure 50.

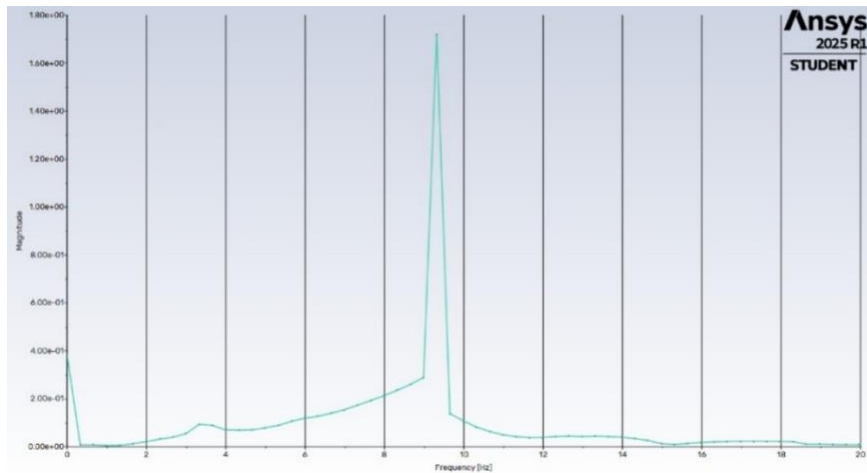


Figure 50 – ANSYS Fourier Analysis for VIV Frequency at 0.5m/s, 15mm Diameter

Repeating the same process for 10 mm at 0.1 m/s, is demonstrated in Figure 51.

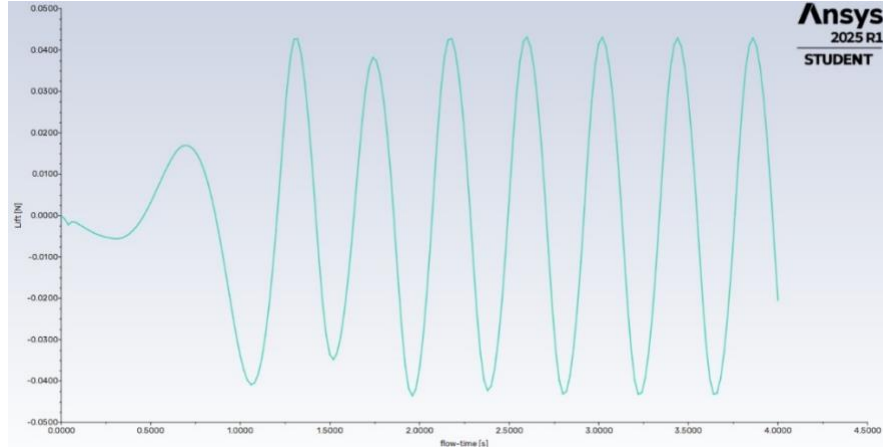


Figure 51 – VIV Lift Force at 0.1m/s, 10mm Diameter

This gives a result of 2.24 Hz as the vortex shedding frequency for a flow rate of 0.1 m/s Figure 52.

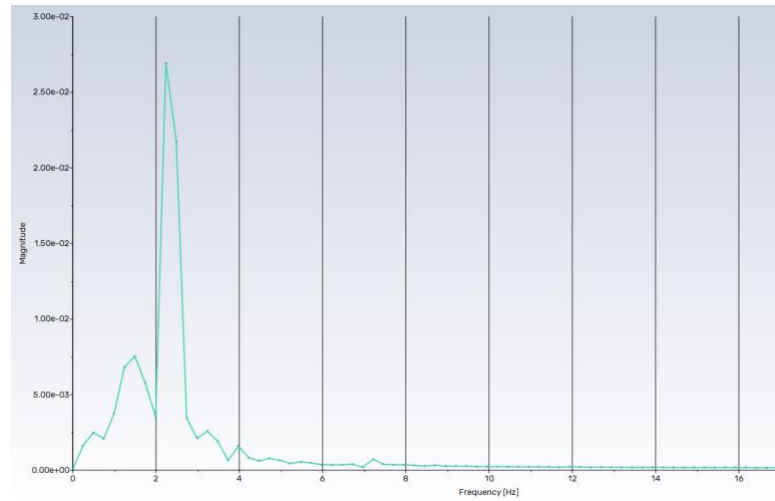


Figure 52 – ANSYS Fourier Analysis for VIV Frequency at 0.1m/s, 10mm Diameter

Repeating the same process for 10 mm at 0.5 m/s, is demonstrated in Figure 53.

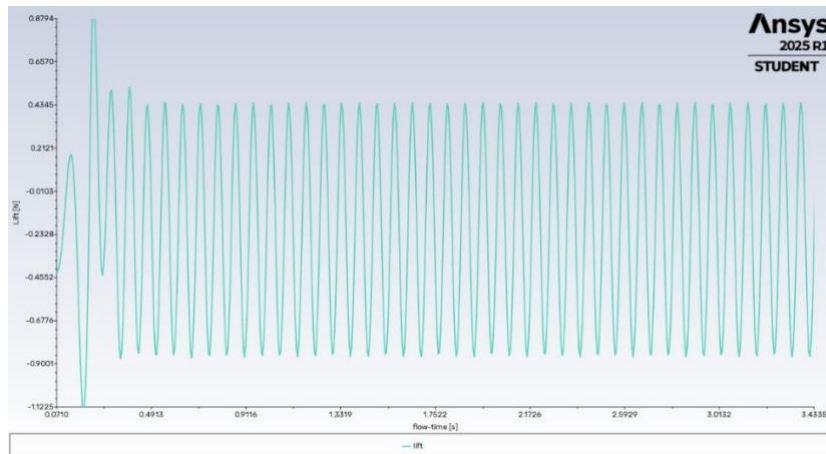


Figure 53 – VIV Lift Force at 0.5m/s, 10mm Diameter

This gives a result of 12.7 Hz as the vortex shedding frequency for a flow rate of 0.5 m/s , demonstrated in Figure 54.

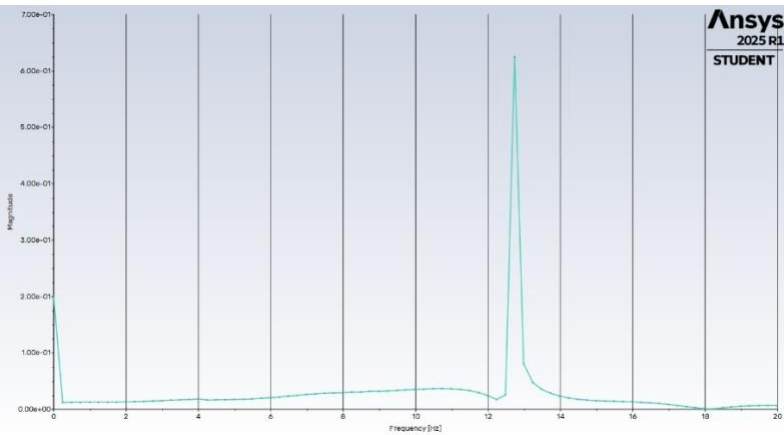


Figure 54– ANSYS Fourier Analysis for VIV Frequency at 0.5m/s , 10mm Diameter

Appendix E

7.1.1 15 mm Diameter Singular PEHs Velocity Contours

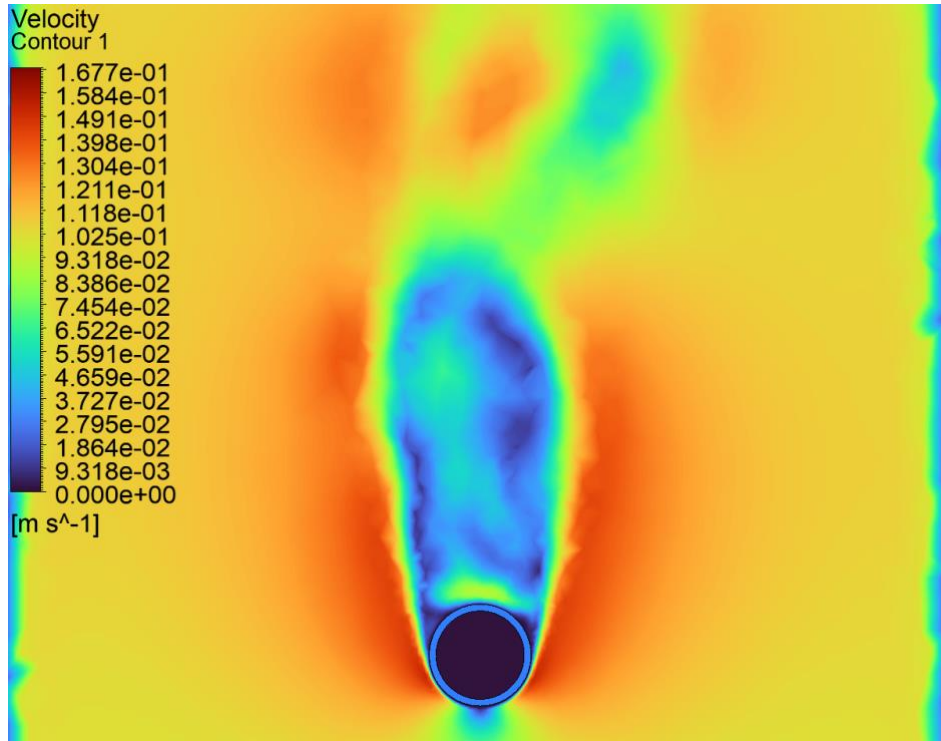


Figure 55 – 0.1m/s Flow Rate, 15mm Diameter Cylinder

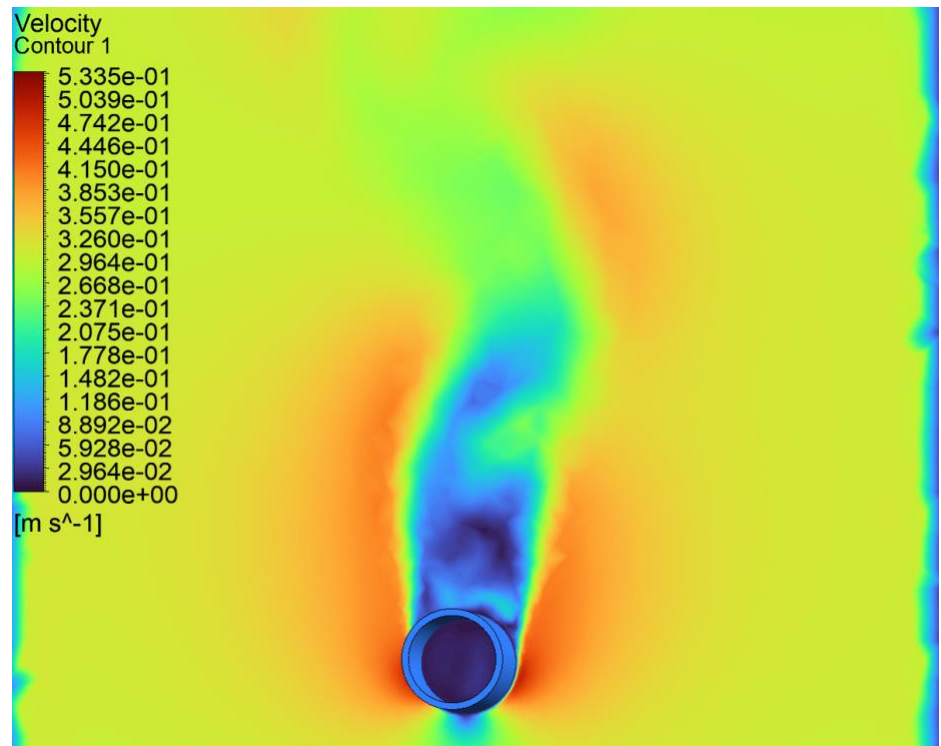


Figure 56 – 0.3m/s Flow Rate, 15mm Diameter Cylinder

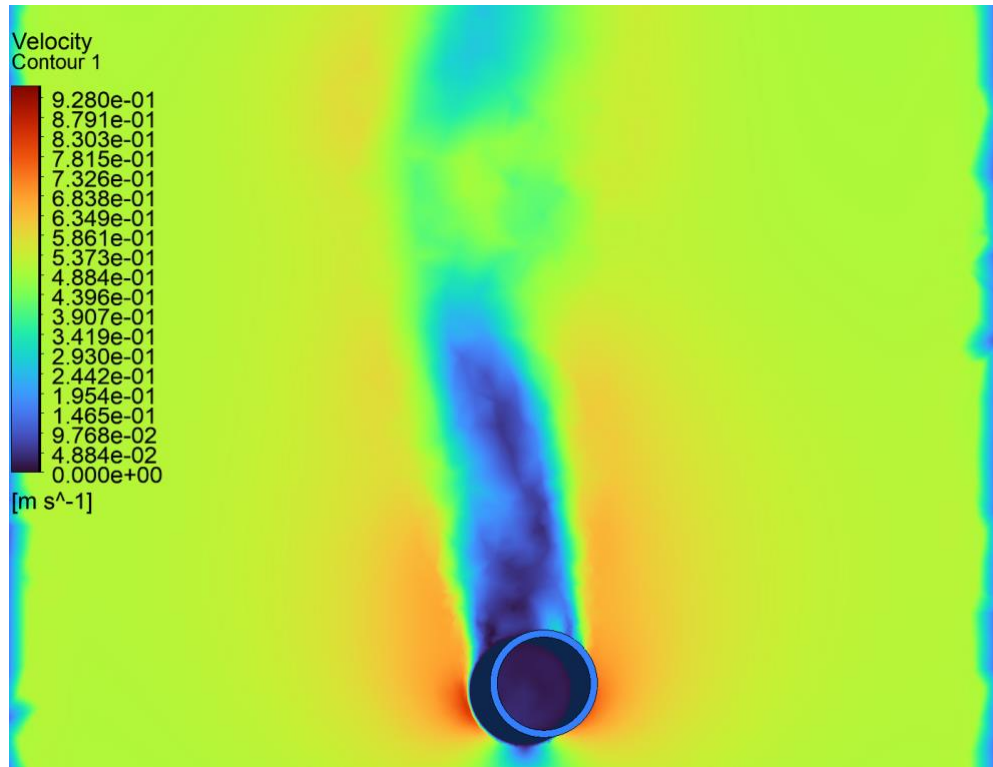


Figure 57 – 0.1m/s Flow Rate, 15mm Diameter Cylinder

7.1.2 10 mm Diameter PEHs Velocity Contours

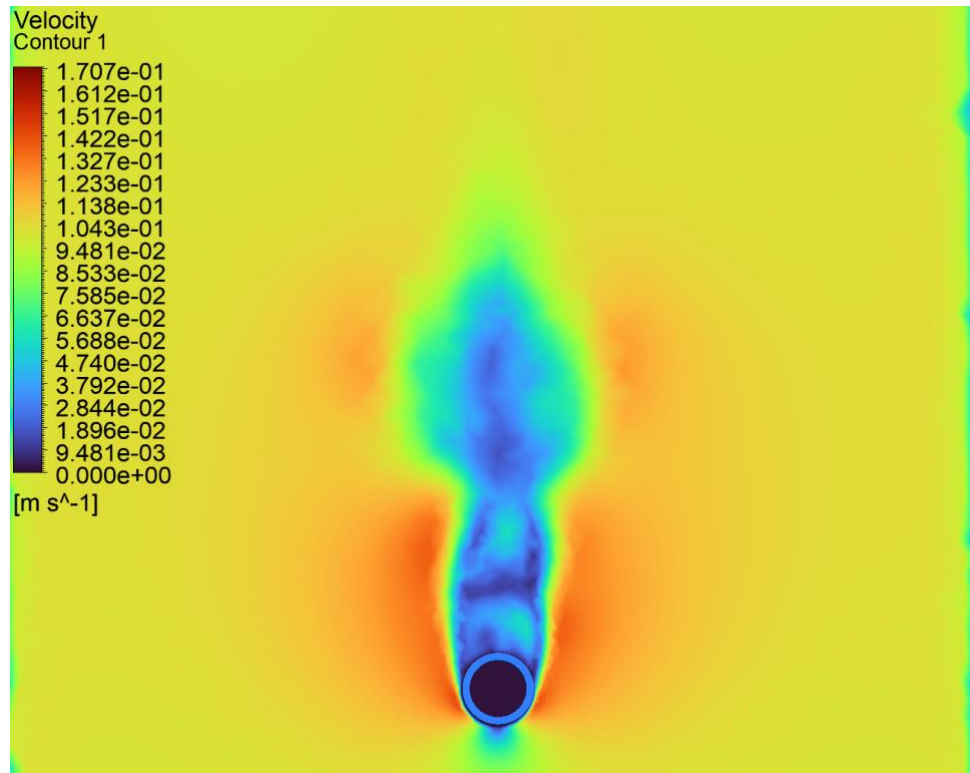


Figure 58 – 0.1m/s Flow Rate, 10mm Diameter Cylinder

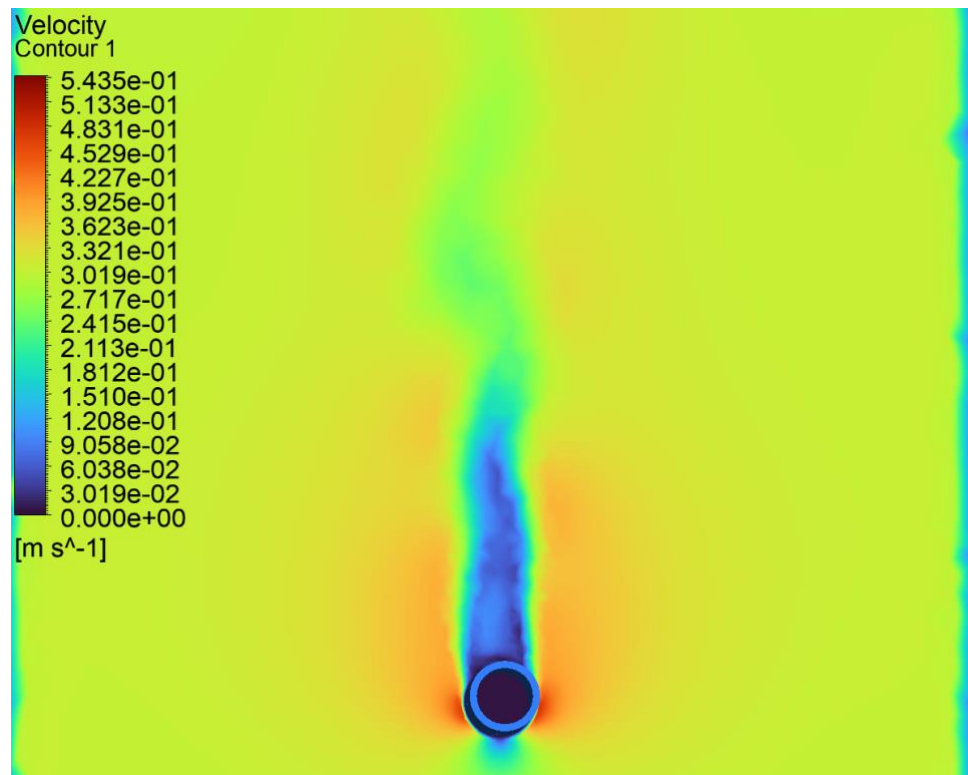


Figure 59 – 0.3m/s Flow Rate, 10mm Diameter Cylinder

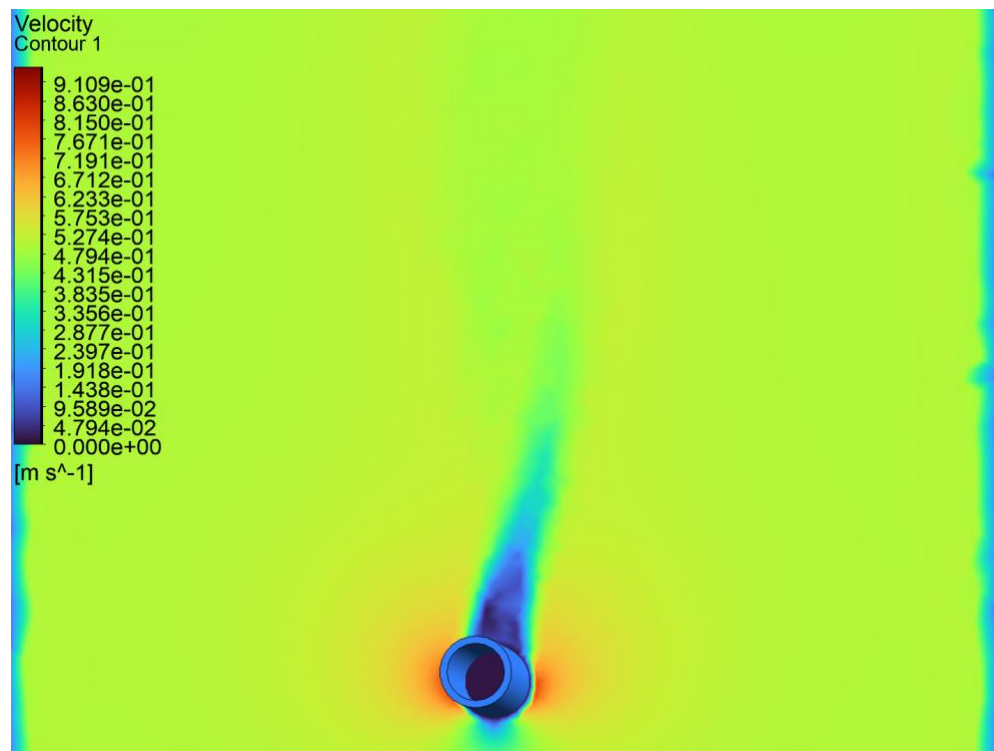


Figure 60 – 0.5m/s Flow Rate, 10mm Diameter Cylinder

Appendix F

7.1.3 2D Separations

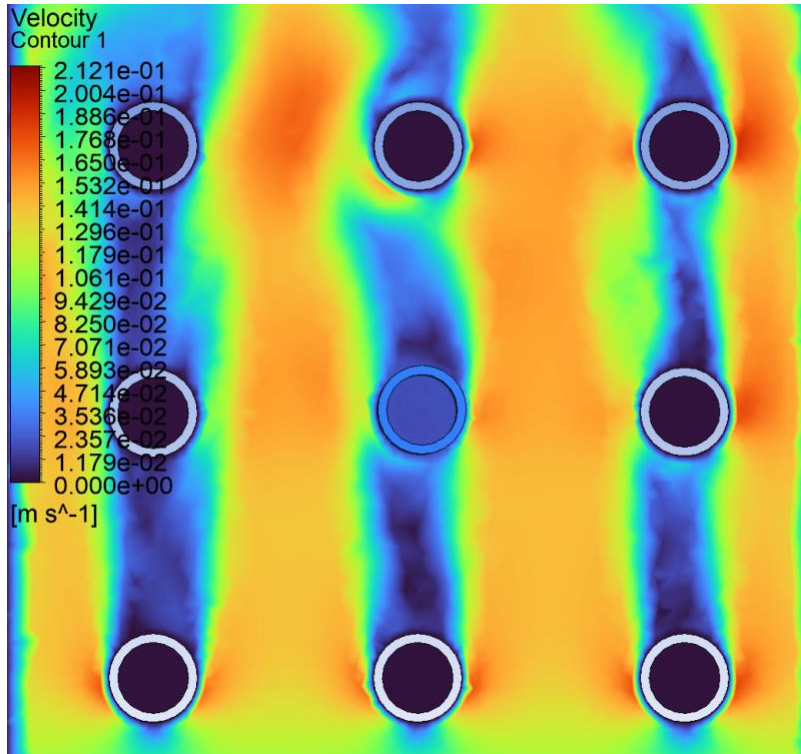


Figure 61 - 0.1m/s Flow rate, 10mm Diameter Cylinder, Three-by-Three 2D Separation

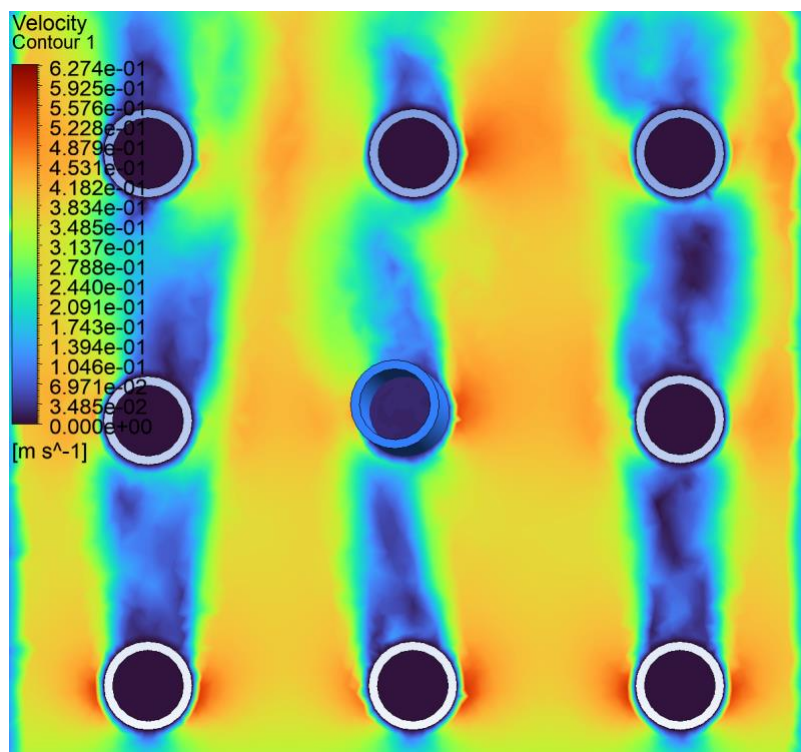


Figure 62 - 0.3m/s Flow rate, 10mm Diameter Cylinder, Three-by-Three 2D Separation

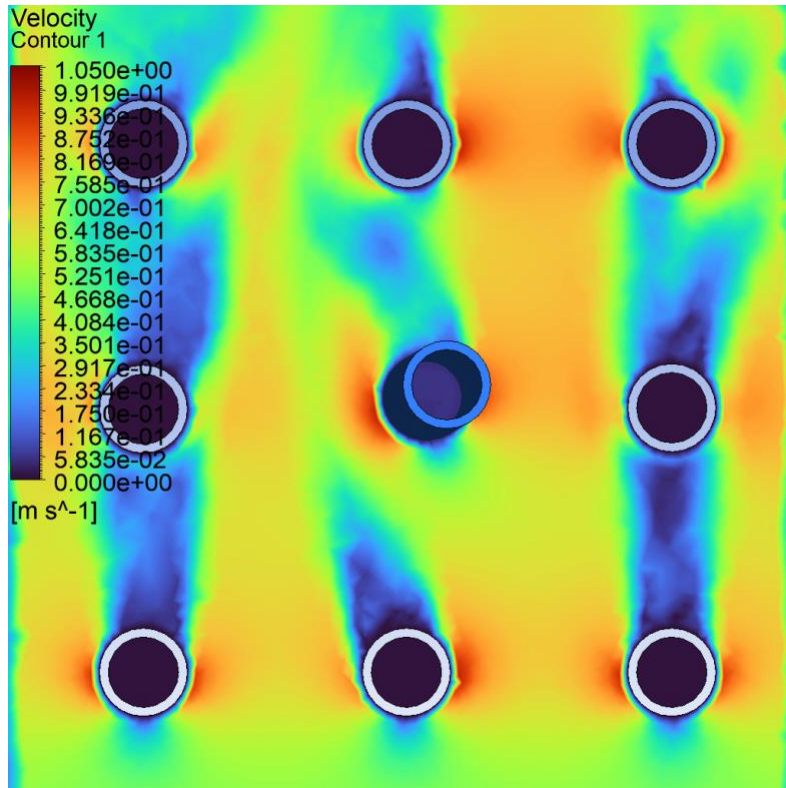


Figure 63 - 0.5m/s Flow rate, 10mm Diameter Cylinder, Three-by-Three 2D Separation

7.1.4 3D Separations

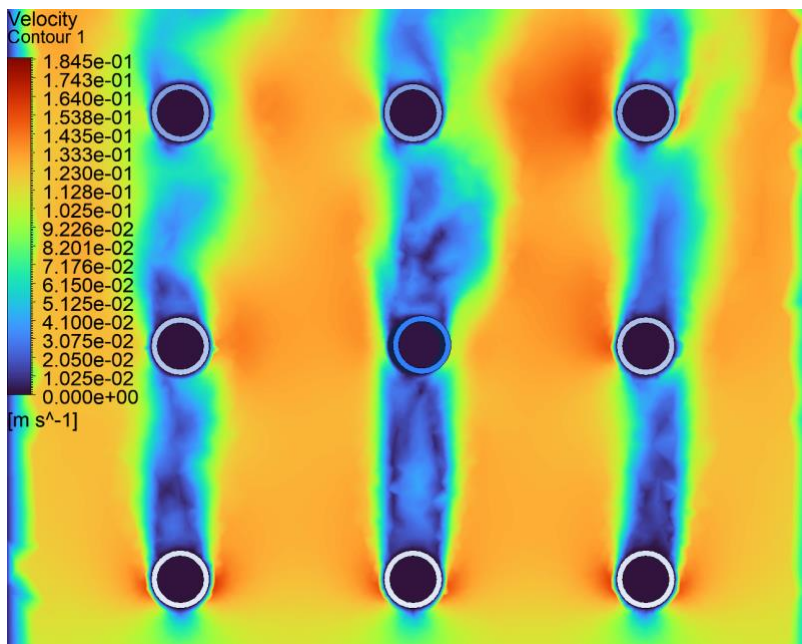


Figure 64 - 0.1m/s Flow Rate, 10mm Diameter Cylinder, Three-by-Three 3D Separation

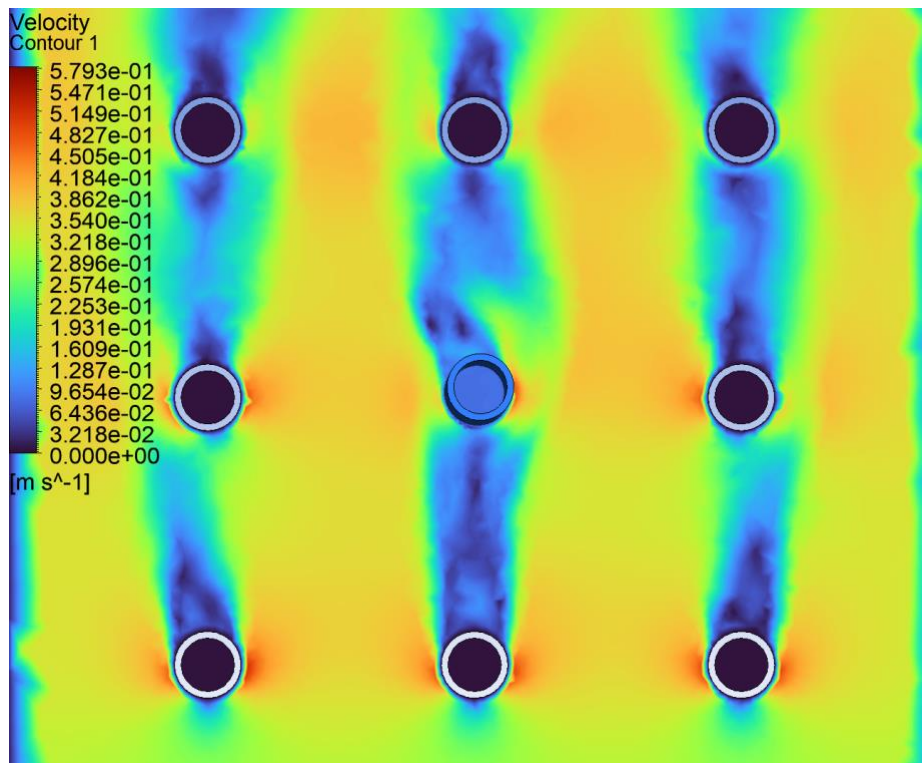


Figure 65 – 0.3m/s Flow Rate, 10mm Diameter Cylinder, Three-by-Three 3D Separation

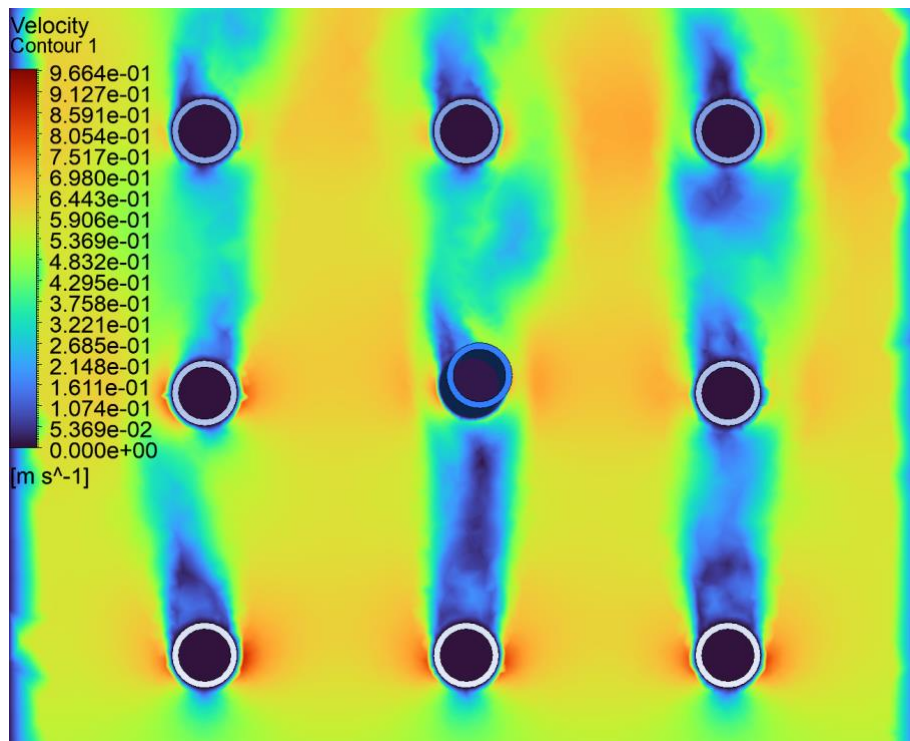


Figure 66 - 0.5m/s Flow Rate, 10mm Diameter Cylinder, Three-by-Three 3D Separation

7.1.5 4D Separations

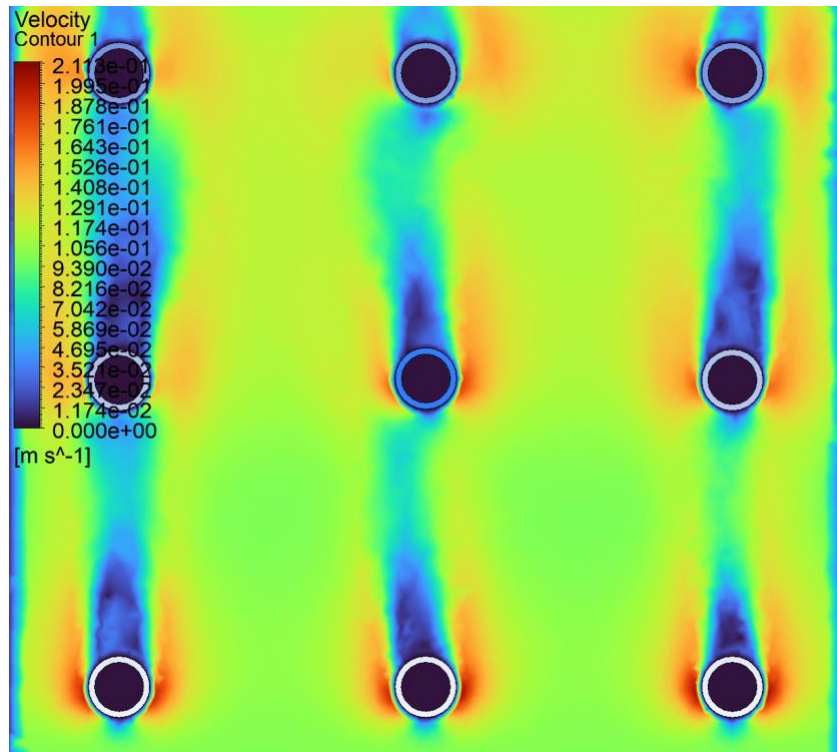


Figure 67 - 0.1m/s Flow Rate, 10mm Diameter Cylinder, Three-by-Three 4D Separation

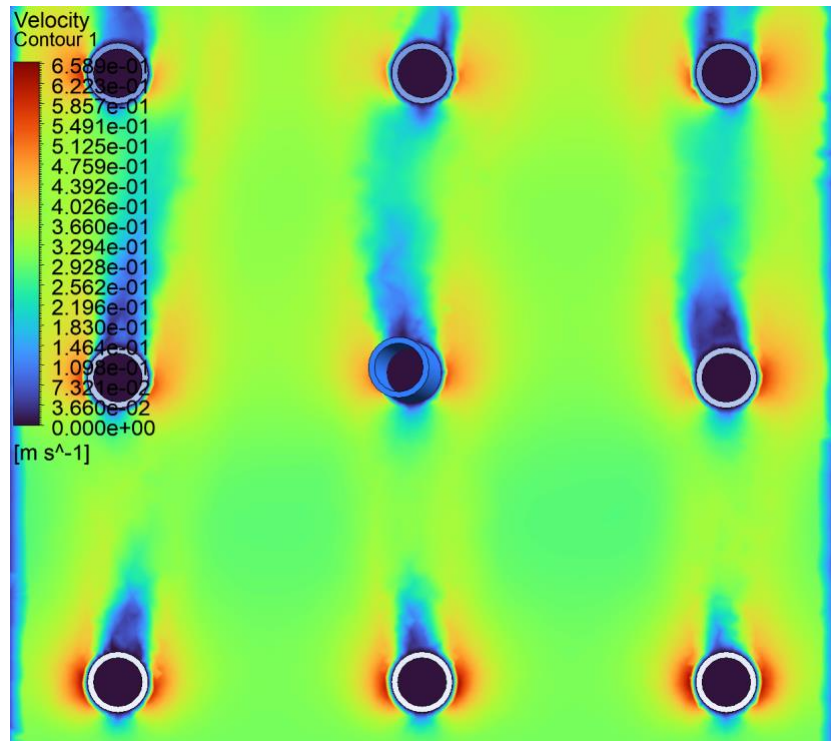


Figure 68 - 0.3m/s Flow Rate, 10mm Diameter Cylinder, Three-by-Three 4D Separation

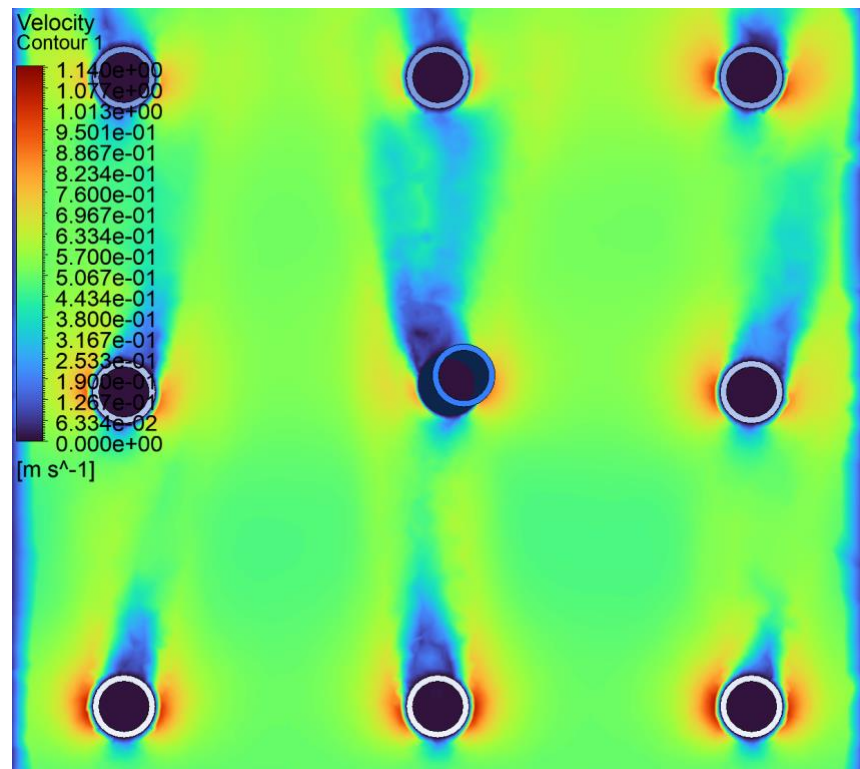


Figure 69 - 0.5m/s Flow Rate, 10mm Diameter Cylinder, Three-by-Three 4D Separation